11-16-2012

Aerosol jet deposition of samarium-doped ceria films

Niranjan Damle

Aerosol Jet Deposition of Samarium-doped Ceria Films

Niranjan Damle

Thesis submitted to the Faculty of the
Rochester Institute of Technology
In partial fulfillment of the requirements for the degree of

Master of Science
in
Industrial Engineering

Thesis Committee
Dr. Denis Cormier
Dr. Marcos Esterman

Department of Industrial and Systems Engineering

11/16/2012

DEPARTMENT OF INDUSTRIAL AND SYSTEMS ENGINEERING

KATE GLEASON COLLEGE OF ENGINEERING

ROCHESTER INSTITUTE OF TECHNOLOGY

ROCHESTER, NEW YORK

CERTIFICATE OF APPROVAL

November 16, 2012

M.S. DEGREE THESIS

The M.S. degree thesis of Niranjan Damle

has been examined and approved by the

thesis committee as satisfactory for the

thesis requirement for the

Master of Science degree

Approved by:

Dr. Denis Cormier, Thesis Advisor

Dr. Marcos Esterman, Committee Member

Abstract

Direct write processes include a range of additive manufacturing technologies. These technologies are employed to fabricate structures by depositing layer upon layer of functional material. The feature resolutions obtained are often in the micron or sub-micron range. This thesis focuses on use of the Aerosol Jet direct write printing process, which shows promise for the fabrication of ceramic films due to its fine feature resolution and flexibility with printing complex features. This study identifies significant process parameters and their relationship to the process output for deposition of Samarium-doped Ceria (SDC) nano-ink. A design of experiments approach is used to generate a model where height and width of the printed tracks are the response variables of interest. Initial feasible operating ranges for each process parameter were identified. Then fractional factorial screening experiments were designed to identify the significant factors affecting the response variables in the study. Two distinct regression equations were generated to predict width and height. Validation experiments were run to confirm the actual values as compared with the predicted ones. For height, the experiment results suggested lack of curvature as well as the standard error and R-squared values were found satisfactory. For width, a higher order model was designed referring to the results of the validation experiment. For the higher order model a three factor three level experiment was considered. The higher order model gives a much lesser standard error and better fit of residuals as compared to the screening model for width. In addition, the study includes a brief discussion on use of Aerosol Jet printing system to manufacture high aspect ratio structures in addition to its application in thin film deposition. The work further demonstrates printing of a high aspect ratio micro-pillar array as a proof of this concept.

Acknowledgement

This thesis would never be complete without the support of several people who in one way or the other have contributed to my work.

First and foremost I would like to thank my family for their unwavering support without which my graduation would never have been possible. Thanks to my father who infused his morals and values in me, which have helped me tremendously in the last few years and will continue to do so. I would like to thank my mother for her unconditional love and support. I will also like to acknowledge my sister who has always been a source of inspiration and support.

I would like to convey my gratitude to my primary advisor Dr. Denis Cormier for his constant encouragement, guidance, and patience, and for providing an excellent atmosphere to learn. I have learnt all that I had hoped to learn in my graduate program and more. I would also like to thank Dr. Marcos Esterman for guiding my research and especially for all his help with the DOE and analysis. This work is also supported by the Heterogeneous Functional Materials (HeteroFoaM) Research Center, funded by the US Department of Energy.

I would like to thank my friends in Brinkman Lab, Anuj, Hrushikesh and Sundar for all the academic discussions and otherwise. Thanks to Pranoti for her love and encouragement over the years. I also owe my friends Ketan, Mihir, Swaraj, and Vidyesh for some memorable times during these two years.

TABLE OF FIGURES

LIST OF TABLES

TABLE OF CONTENTS

1. Introduction

This study explores the use of Aerosol Jet printing for synthesis of heterogeneous functional materials (HetroFoams). These are materials that find applications in various energy systems such as fuel cells, batteries, and membranes. The functional materials can be fabricated in thick or thin, and porous or gas tight films depending on the application. The properties of these fabricated materials, such as microstructure, size, composition and orientation, depend on their intended functionality. Processes such as tape casting, screen-printing, and freeze tape casting, to name a few, are used to fabricate these functional films. Aerosol Jet printing is an example of direct-write printing, which is a newer category of deposition techniques suitable for depositing thin functional films as well as structured films of functional materials.

Samarium-doped ceria (SDC) is the functional material used in this study. SDC is used in ceramic membranes, which find applications in solid oxide fuel cells (SOFC). SOFC cells are typically either zirconia or ceria based. The ceria-based cells often use SDC as the electrolyte material. This SDC layer can also serve as a base or foundation for the porous cathode. Often an SDC matrix or SDC layer is coated or infiltrated with a cathode material of choice. Shao et al. [Shao and Haile, 2001] use an SDC electrolyte and an SDC cathode matrix that is infiltrated with strontium samarium cobaltite (SSC). Simner et al. (2003) demonstrated the addition of an SDC layer between a YSZ electrolyte and an LSF cathode as it marginally enhances the ionic conductivity of the cathode. So considering the applications of SDC, fuel cells and specifically solid oxide fuel cells are briefly reviewed.

1.1. Fuel Cells

Fuel cells are one of the oldest known types of energy converting devices. The invention of fuel cells as an electrical energy conversion system is attributed to Sir William Grove. The principle behind its working was discovered by Christian Friedrich Schonbein [Ormerod, 2002].

Fuel cells convert energy in the form of gasses or liquids into electricity. Fuel cells convert chemical energy of a fuel to electricity by an electrochemical reaction. As the fuel cell is an electrochemical cell, each electrochemical reaction is characterized by the thermodynamic equilibrium potential that is described by the Nernst equation [Carrette et al., 2001]. Different fuel cells use a variety of fuels, the most popular being hydrogen. They generally produce much lower sulfur and nitrogen oxide emissions, hydrocarbon pollutants, and CO_2 than are generally produced in conventional electricity production. Such emission factors, and concern about environmental consequences of using fossil fuels, have influenced many developments in fuel cells. Various types of fuel cells have been developed that operate with a similar principle.

1.2. Solid Oxide Fuel Cells (SOFC)

Solid oxide fuel cells, as the name implies, use a solid ceramic inorganic oxide as its electrolyte. Yittria-stabilized zirconia (YSZ) and samarium-doped ceria (SDC) are the two most prevalent electrolyte materials. The electrolyte acts as a conductor for oxide ions at temperatures between 600-1000^{o}C [Ormerod, 2002]. They generally run on hydrogen as the fuel and air as an oxidant. They produce water as a byproduct. The SOFC has three basic components - a cathode where oxygen is reduced to oxygen ions, a solid electrolyte that acts as a passage for the oxygen ions, and an anode where the transported ions react with the fuel to form water and electricity.

SOFC's are attributed with high-energy conversion efficiency that can reach up to 65%. Hence, they find many applications in electric power generation systems. SOFCs generally operate at very high temperatures. There are performance advantages to operating at this range, as they provide high quality waste heat and activate reforming and oxidation of hydrocarbon fuels in the presence of catalysts.

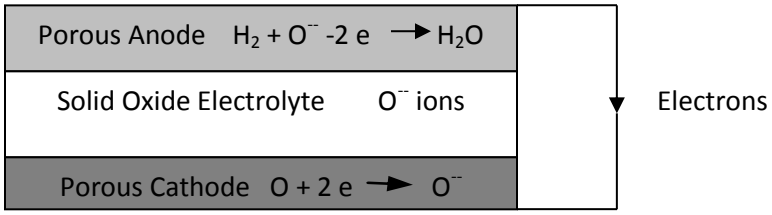

Figure 1: SOFC model

1.3. SOFC Working Principle

Figure 1 depicts the working principle of a typical SOFC running on hydrogen. The solid ceramic electrolyte allows oxygen atoms to be reduced on the porous cathode surface. They are reduced at the cathode/electrolyte interface where oxygen atoms become oxygen ions. The reaction observed at the cathode interface is $\frac{1}{2}\ O + 2\ e \rightarrow O^{--}$.

These oxygen ions are transported through the ceramic electrolyte to the porous anode. Here the conducted ions react with the fuel, mainly hydrogen. The $O^{—}$ ions combine with H_2 at the electrolyte/anode interface to form water, $H_2 + O^{—} \rightarrow H_2O + 2\ e^{-}$. These electrons travel through the external circuit from the anode to the cathode.

The overall reaction in the SOFC is $H_2 + \frac{1}{2}\ O_2 \rightarrow H_2O$.

1.4. SOFC Materials

The working conditions of SOFC's present challenges with respect to the selection of materials used in their construction. For example, the anode and cathode must have high electronic conductivity. They must be chemically and structurally stable at high temperatures and should

possess minimum reactivity with other cell components. The thermal expansion coefficients between different cell component materials must be closely matched. For electrode materials, sufficient porosity is required for the transport of gasses and air to their respective electrode/electrolyte interfaces. They are also required to carry away the byproducts from their respective interfaces.

Many commercially available SOFCs use a yittria-stabilized zirconia (YSZ) electrolyte, a strontium doped lanthanum manganite cathode, and a nickel- yittria-stabilized zirconia anode. For cathodes, lanthanum manganite LaMnO3 doped with strontium is found to improve its electrical conductivity. The doped material is also found to have better thermal expansion and chemical properties [Singhal, 2000]. A cross-section of a commercial SOFC is shown in Figure 2 below.

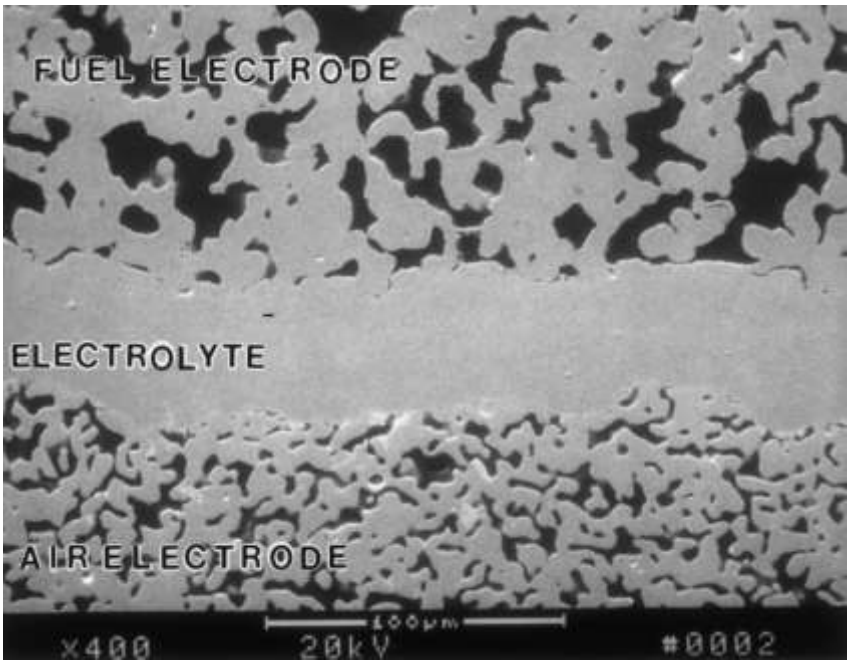

Figure 2: Microstructure of cross-section of Westinghouse SOFC [Singhal, 2000]

1.5. SOFC Polarizations

Polarization is a voltage loss that occurs in a cell. There are three different polarizations that are studied for cells. They are ohmic polarization, activation polarization, and concentration polarization.

1.5.1. Ohmic Polarization

Ohmic losses come from the known fact that all matters offer a resistance in the path of an electric charge. The relationship between voltage drop and current density can be described by the material property of resistivity. Similar behavior is observed in an SOFC cell. Due to the

SOFC's ohmic resistance, a voltage drop is observed. The resistance can given by, *H* ohm = *ρ(l/A)*, where *ρ* is the resistivity of the material and *l* is the film thickness. In SOFC's, the most significant contribution of ohmic losses come from the electrolytes. Chan et. al. (2001) indicate that after ohmic polarizations in the electrolyte, the cathode polarizations are the most important for obtaining the lowest possible cell voltage drop and improved current density. The cathode ohmic polarizations become even more significant in the currently used electrode supported SOFCs. In electrode-supported cells, electrolyte films of 5 to 30 microns are used, thus reducing the effect of ohmic polarization in the electrolyte.

1.5.2. Activation Polarization

Electrode reactions involve transfer of a charge to the solid oxide electrolyte. At the cathode, the charge transfer consists of conversion of an oxygen molecule to oxide ions.

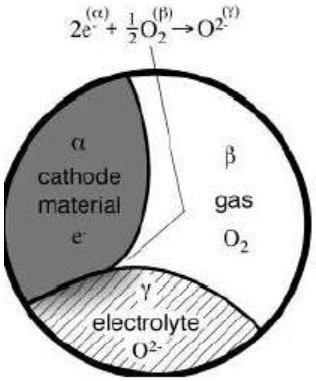

Figure 3:Triple phase boundary [Adler, 2004]

The electrons flow to an electrically active site, known as a 'triple phase boundary', which exists at the electrode/electrolyte interface. The triple phase boundary is a region between the cathode surface, the electrolyte material, and the gas (Figure 3). The cathode material (α) meets with an electrolyte phase (γ) along an interface. This interface is also adjacent to a gas phase (β) which contains oxygen within the electrode pores. Here the solid electrode provides a path for electrons, and the electrolyte phase acts as an ionic path where the available oxygen is reduced. Oxygen is always reduced near this α/β/γ interface known as the triple phase boundary. The performance of the SOFC largely depends on the geometric length of this triple phase boundary. The reaction rate within a cell is also affected by the triple phase boundary characteristics.

A decrease in the rate of reaction or the passage of current can produce a loss in voltage. This loss is activation polarization observed in cathodes. The reaction rate depends on the triple phase boundary length. The geometric parameters such as surface area, porosity, electrode thickness and exact distribution of all phases strongly affect the reaction rate, hence affecting the activation losses [Adler, 2004]. Considering these properties while fabricating cells is imperative in order to scale the overall performance of a SOFC stack.

1.5.3. Concentration Polarization

Concentration polarization occurs in a cell due to any fluctuations in the flow of gasses to the reaction sites. This form of polarization is mainly related to the mass transport of gasses in the cell, hence it affects both electrodes. Concentration losses can significantly reduce the performance of a fuel cell. The flow of gasses through the electrode largely depend on physical characteristics such as microstructure, tortuosity, porosity, pore size, and thickness of the electrode. Concentration losses can be reduced by using high surface area electrodes and thinner electrodes that shorten the path of the flowing gas to the sites.

1.6. Ideal Characteristics for a Deposited Film

Considering earlier discussions in the study, we analyze the ideal characteristics for a fabricated HeteroFoam thick film.

- Very thin cross section for minimal ohmic losses
- Strength to withstand thermal expansion and contraction
- Sufficient porosity to scale transport of gasses at the reaction sites
- Suitable microstructure of pores with controlled tortuosity to speed the reaction rate
- Higher surface area of the film, especially near reaction sites

Performance of a fabricated HeteroFoam film is highly dependent on its thickness, porosity, surface area and its microstructure. Therefore, the processing methods used in preparing them are very important in determining their performance.

1.7. Review of Process for Fabrication of Functional Films

This section describes various processing and fabrication methods used to deposit heterogeneous functional materials and thick films. Sections for each process used are included in the study.

1.7.1. Screen Printing

Screen printing is the most widely used process for fabricating ceramic planar layers of an electrolyte, anode or cathode in an SOFC. In screen printing, a porous mesh is stretched over a frame, acting as the screen. Areas of the same are blocked to form a pattern that is to be printed on the substrate. A paste-like ink is placed on the screen and is filled in the mesh openings. A squeegee is used to lower the mesh on the substrate that releases the ink on to it. Through screen printing, dense or porous layers can be fabricated.

Piao et al. (2008) demonstrated preparation of LSM cathodes by mixing LSM powder with selected binder and organic solvents. The selection of the binders affects the microstructure of the cathode layers. A porosity of 30-40% was obtained. Selection of mesh screen also affects the microstructure greatly. A lower sintering temperature is preferred, as higher sintering temperatures increase the density of the films and significantly decreases the triple phase boundary length. The resultant thickness of the printed layer by screen printing is approximately 20 microns. The microstructure of the printed cathode can be seen in Figure 4.

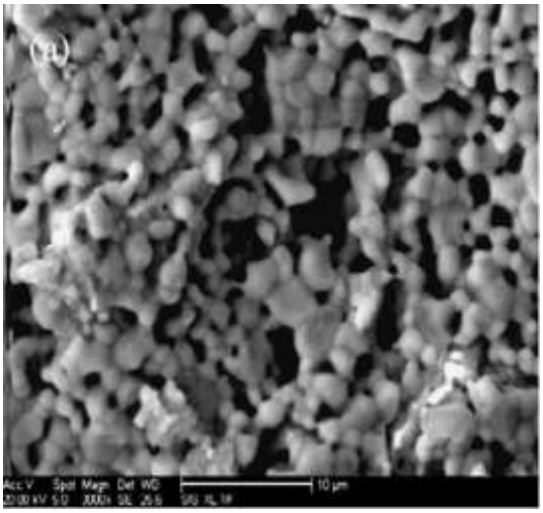

Figure 4: SEM micrograph of a LSM-YSZ composite cathode fabricated by screen-printing [Piao et al., 2008]

1.7.2. Tape Calendaring

Tape calendaring is the process of forming one continuous sheet by pressing multiple planar tapes between two or more rollers as seen in Figure 5. It is widely used to connect the prefabricated functional layers with the substrate. It is an easily scalable and cost effective way of producing multi-layer cells.

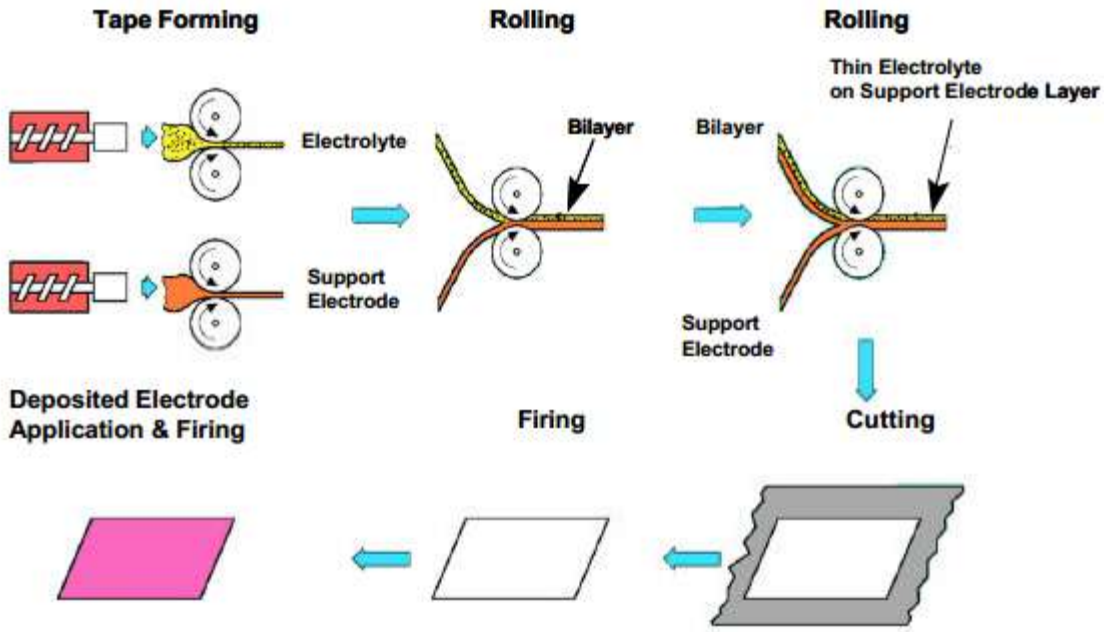

Figure 5: Fabrication sequence while tape calendaring [Minh & Montgomery, 2004]

In producing SOFCs by calendaring, first a half-cell is produced by combining one electrode and electrolyte. This cell is then sintered and again combined with another electrode in a second step to form a complete cell. This process is mostly used with two different tapes of similar thickness, hence it is difficult to produce cells with thin functional layers on a relatively thicker substrate.

1.7.3. Spin Coating

Spin coating is used to obtain uniform coatings for a defined thickness on a substrate. The process of spin coating consists of accelerating a liquid on a rotating disc. It utilizes centrifugal and viscous forces to form a required uniform coating. The centrifugal forces make the liquid on the spinning disk spread out radially with respect to the center of rotation. The resulting film is then dried. The coating thickness can be controlled by varying the spinning speed, spinning time and viscosity of the liquid. Film thickness of a few microns is obtainable by screen printing.

Peng et al. (2005) successfully spin coated YSZ films with 12 coating layers at a speed of 1000 rpm resulting in a 20 micron thick film. The number of coating cycles and the spinning rate most significantly affected the film thickness. An SEM micrograph of the resulting microstructure is shown in Figure 6.

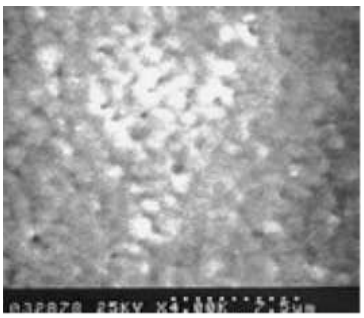

Figure 6: SEM micrograph of a spin coated YSZ film [Peng et al., 2005]

1.7.4. Dip Coating

Dip coating is often used to produce thin planar or three-dimensional structures. In dip coating, a substrate is dipped into a liquid suspension. It is then withdrawn at a controlled speed to get the required coating thickness as depicted in Figure 7. Typical thicknesses observed from a single suspension step can be anywhere from 2 to 10 microns [Scriven, 1988]. Multiple coatings are needed to produce the required thickness. This has mostly restricted its use for laboratory purposes. The major parameters observed to be significant during dip-coating are the suspension viscosity, the time of coating, the powder loading of the suspension, the coating temperature, and the speed with which the part is moved through the suspension [Xia et al., 2000].

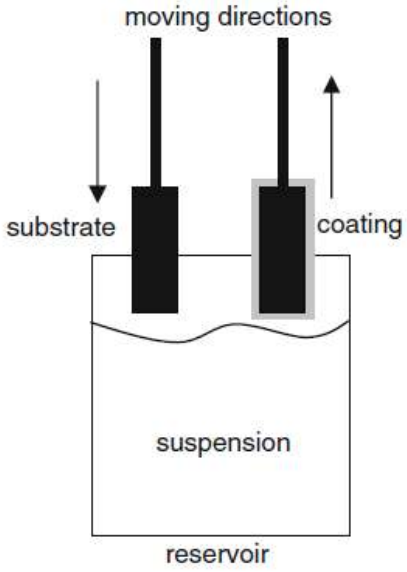

Figure 7: Vertical dip coating [Scriven, 1988]

YSZ films were dip coated by Peng et al. (2000) resulting in a film thickness of 32 microns after four coating steps. The resulting microstructure of the film is shown in Figure 8.

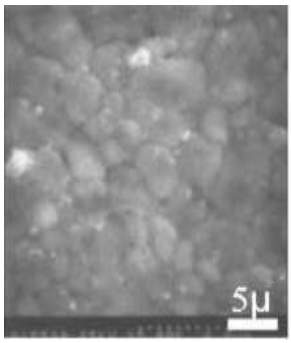

Figure 8: SEM micrograph of a dip coated YSZ film [Peng et al., 2000]

1.7.5. Extrusion

Extrusion is used to fabricate continuous structures having elongation in one direction. Extrusion is a very cost effective way to produce continuous cross-sectional features such as tubes and rods, and hence they are widely used to fabricate tubular SOFC designs.

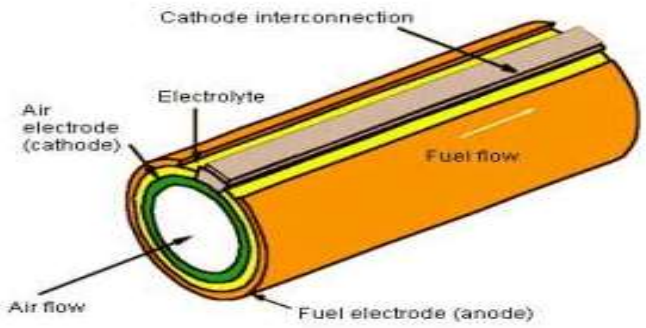

Figure 9: Tubular SOFC [Carrette et al., 2001]

With this process, a paste like ink is extruded through a die. The paste must maintain a flow and should have enough green strength for the ceramic extruded tube to remain unharmed during handling. Additives are extremely important in this process for maintaining green strength. Following extrusion, the tubes are cut to the required length. They are also deboned and sintered before other functional layers are applied. The resulting microstructure of extruded tubes is shown in Figure 10.

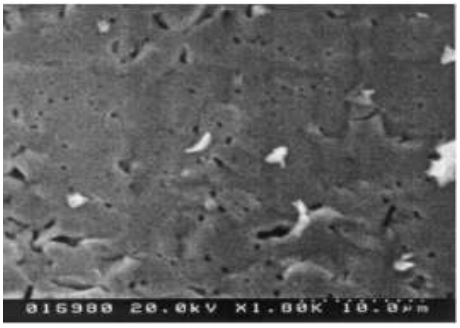

Figure 10: Microstructure of cross-section of an extruded tube [Du et al., 2000]

1.7.6. Plasma Spraying

Conventional plasma spraying is commercially used to fabricate SOFC cells. In plasma spraying, particles of the material to be coated are introduced through a carrier gas in a plasma jet produced from a dc plasma torch. The particles in the gas are rapidly accelerated in the plasma jet where they melt and are flattened onto a substrate.

Li et al. (2005) demonstrated plasma spraying of an YSZ film onto a polished stainless steel substrate. Multiple coatings were sprayed to get a film thickness of about 30 microns, where each pass deposited approximately 0.8 microns. A microstructure of the coating is shown in Figure 11.

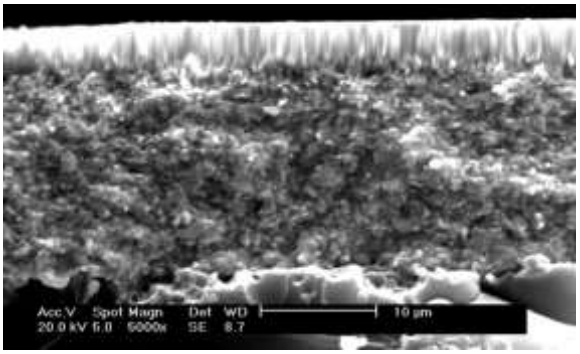

Figure 11: Plasma sprayed YSZ coating [Li et al., 2005]

1.7.7. Tape Casting

Tape casting is widely used to manufacture thin ceramic porous or dense supports. It is mostly used to make mechanical bearing supports for planar SOFC designs. The thickness range produced is typically between 100 to 800 microns post firing [Mistler and Twiname, 2000].

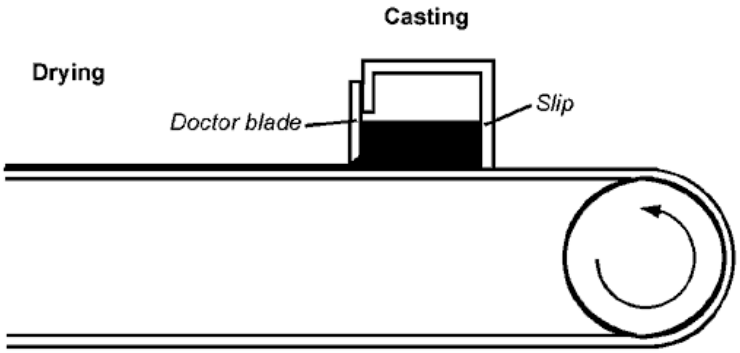

Figure 12: Tape casting process [Mistler and Twiname, 2000]

In tape casting, the slip is transferred via tubing to the reservoir behind the doctor blade. A fixed level of slip is always maintained during a continuous production run. The slip is generally prepared by mixing ceramic powders with solvents and organic additives. The required porosity is obtained by mixing organic additives or pore formers to the slip. The slip is deposited on the transport tape as the tape moves below the doctor blade. The doctor blade is adjusted to give the slip layer a required thickness across the width of the tape. Then the tape is dried in a drying chamber and cut for use.

Boaro et al. (2003) demonstrated fabrication of YSZ ceramic layers using tape casting. It was found that the resulting pore structure could be controlled by varying the type of pore former used, pore former particle size, shape, and pore former loading in the slip. This process can obtain a film thickness as small as 10 microns. It is also seen that the pore former mixture in the slip acts as template for the resulting microstructure. However, this process limits grading capability. The resulting microstructure of a tape casted film is shown in Figures 13 and 14.

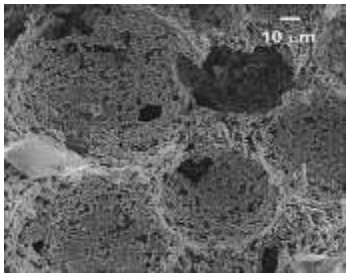

Figure 14: YSZ with Graphite 21 wt. % & PMMA 28 wt. % [Boaro et al., 2003]

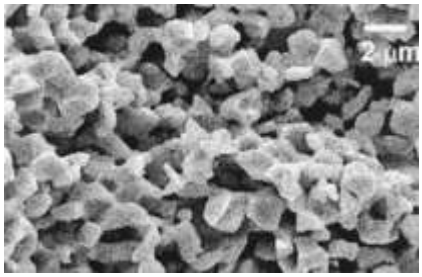

Figure 13: YSZ made from NiO-YSZ [Boaro et al., 2003]

1.7.8. Freeze Tape Casting

The freeze tape casting process is a combination of the tape casting and freeze drying processes. It allows one to form and control pore structures in the cast tape. Freeze tape casting allows tailoring of continuously aligned graded pores through the entire cross-section of the film. It uses

a manufacturing apparatus similar to that of tape casting as depicted in Figure 15. The slip is typically tape cast onto Teflon coated Mylar carrier film. A thermally isolated freezing bed beneath the film allows for unidirectional solidification of the ceramic slurry after tape casting. The freezing bed is maintained at a constant temperature, and a constant feed rate is applied to the film. This ensures a continuous and directional solidification, which creates straight long-range pores in direction of the moving film.

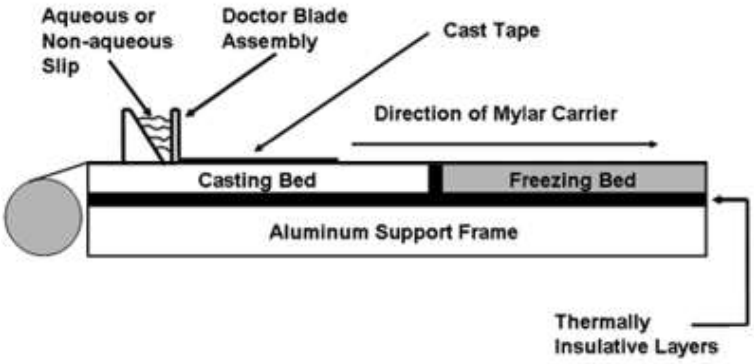

Figure 15: Freeze tape casting process [Sofie, 2007]

Freeze tape casting has been used to fabricate functionally graded and continuously aligned pore structures as SOFC electrodes. Ceramic material with thick substrate sections of approximately 500-1500 microns have been fabricated by this process [Sofie, 2007]. In freeze tape casting, the pore structure can be tailored by varying the solid loading fraction and the freezing bed temperature. During solidification of the deposited ceramic slurry, the solid particles are rejected to the boundary between solvent crystals that form during freezing. These solvent crystals are then freeze-dried for solvent removal. The volume previously occupied by solvent crystals therefore ends up as columnar pores or voids. The pores can extend throughout the entire cross section of the film.

As discussed earlier, varying the solids loading and freezing temperatures allows one to produce unique long columnar pore morphologies in the ceramic substrates. These substrates also serve as effective gas transport mediums with a very low tortuosity. The path traveled by gas molecules is much lower as a result. A SEM micrograph of an SOFC with a NiO-YSZ freeze tape cast anode is shown in Figure 16.

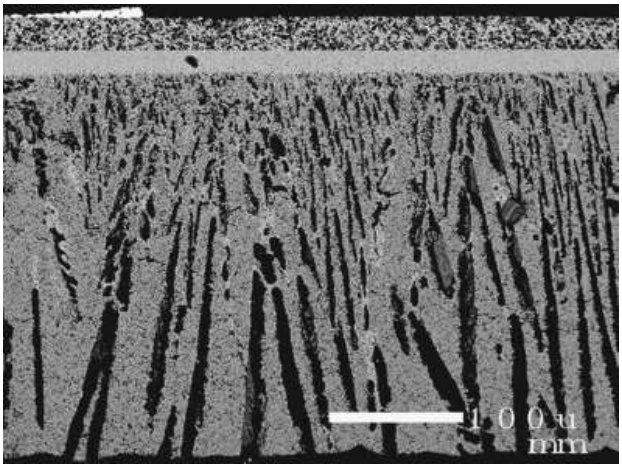

Figure 16: NiO-YSZ freeze tape cast SOFC anode [Sofie, 2007]

Summarizing for the processes reviewed, the process selected for fabrication of functional layers affects its physical characteristics such as porosity and microstructure. Table 1 provides a brief comparison of conventional processes used to fabricate functional films. In most of the processes, the resulting porosity is sufficient and provides pathways for the flow of gases and the required active sites. These processes are also easily scalable for building up the SOFC layers of electrolyte or electrodes. However, tailoring and controlling the porosity and the resulting microstructure is a difficult task. The amount of porosity can be controlled by varying the amount of pore former. The size of pores can also be influenced through selection of pore former particle size. Most of the reviewed processes are limited in terms of structural and functional grading of films. Plasma spraying allows one to grade the pore structure, although the range of porosities obtained are limited considering the applications in hand. Freeze tape casting is able to produce long columnar pores throughout the cross-section of the printed SOFC layer. It is a promising method for fabricating SOFC substrates allowing effective functional as well as structural grading through the thickness of the film. The thickness of the printed layer is one of the constraints in this process, as very thin substrates (<30 microns) are difficult to produce with this process. It is hard to locally control the chemical composition with most conventional thick film processes.

Table 1: Comparison of fabrication techniques [Flesner, 2009]

Fabrication Technique	Grading Capability	Cost	Porosity	Thickness
Screen printing	Poor	High	0-60	>8 µm
Tape calendaring	Poor	Low	N/A	N/A
Dip coating	Poor	High	0-60	>10 µm
Extrusion	No	Low	0-60	N/A
Plasma spraying	Yes	Low	5-20	>particle size
Tape casting	Poor	High	0-60	>7 µm

1.8. Problem Statement

This research explores the use of a relatively new Aerosol Jet printing process. The Aerosol Jet process has been used to fabricate SOFC cells with promising results. To build upon the previous work involving synthesis of HeteroFoams for applications such as SOFC's, this research focuses on the fabrication of thick films via Aerosol Jet printing. Aerosol Jet printed features often tend to spread on the substrate, and hence it is difficult to print high aspect ratio structures. This study therefore examines the process parameter relationships that dictate the extent to which printed line height and width can be controlled. The study concludes with a demonstration of Aerosol Jet deposition of high aspect ratio pillar arrays that serve as one example of a HeteroFoam material.

The primary objectives of this study are as follows:

1. To determine process parameters that enable printing of narrow width features
2. To build a parameter model, which enables us to set the system settings as per the required feature properties
3. To fabricate high aspect ratio structures using the Aerosol Jet process

2. Methodology

2.1. Direct Write

Direct write processes are additive manufacturing technologies in which functional inks are selectively printed upon a substrate. The feature resolutions obtained are often in the micron or sub-micron ranges. Direct write technologies can be used to build a variety of structures on planar or conformal substrates.

2.1.1. Aerosol Jet Printing

Aerosol Jet printing is a direct write technology commercialized by Optomec. The process uses aerodynamic focusing of an aerosol stream onto the substrate. The system consists of an atomizer where a mist is generated by atomizing the source material. The aerosol stream is then refined in a virtual impactor, thus resulting in a dense aerosol. A collimating sheath gas inside the deposition head then focuses the dense aerosol stream. The focused aerosol is then directed onto a computer numerically controlled substrate through a nozzle. The printed structures can be sintered by an attached laser or by other sintering methods. The printed features can be as small as 10 microns wide, and the layer thickness can be as thin as 100's of nanometers. The system can process a wide range of commercially available inks including polymers, metallic inks and ceramic inks. The system is capable of printing multiple materials through co-atomization. These materials can also be graded to the required proportions.

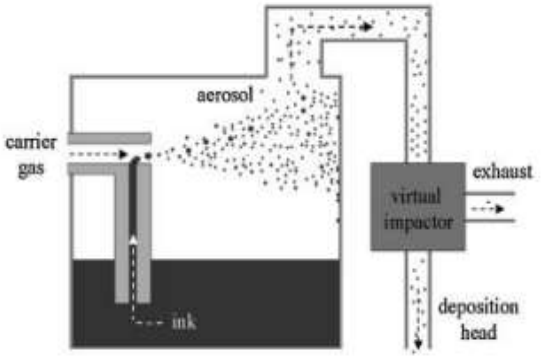

Figure 17: Aerosol Jet process [Mette et al., 2007]

The Aerosol Jet system consists of an atomizer unit, a virtual impact unit, and a deposition head that includes a ceramic nozzle. In the atomizer unit, a cup contains an ink that can be a particulate suspension of the solid material to be printed. As seen in Figure 17, a metallic housing is threaded air tight with the atomizer cup. The metallic housing consists of a hollow metal shaft to which the atomizer unit is threaded. The atomizer unit is threaded and adjusted so as the bore in its bottom face is immersed in the ink to be printed and the bore on the side of the atomizer protrudes out of the ink. The atomizer is a cylinder having a micro-machined bore that

is aligned with the hollow metal shaft secured in the housing. When a carrier gas (e.g. nitrogen) is passed through the atomizer, the Venturi effect pulls the ink up through a tube and allows a mist to be formed. This aerosol mist is carried to a virtual impactor unit. The virtual impactor bleeds off excessive carrier gas and densifies the aerosol stream. This is done to allow flow of the material through a nozzle that is typically in the 150-300 micron inner diameter range. The dense stream enters the nozzle through a deposition head where it is surrounded by a sheath gas. The sheath gas is a collimating gas that avoids any settling of aerosol droplets on the nozzle sides in order to avoiding clogging. It also focuses the aerosol stream further to control the width of the resulting aerosol.

Aerosol Jet printing is being explored for SOFC fabrication due to certain advantages of feature resolution, flexibility, patterning, etc. Sukeshini et al. (2011) have successfully used Aerosol Jet printing to fabricate SOFC layers of a composite LSM/YSZ cathode current collection layer and LSM cathode layer. LSM and YSZ were atomized simultaneously in two different atomizers to produce a 1:1 wet ratio. An LSM/YSZ current collection layer was printed by mixing YSZ and LSM on the fly. Then an LSM layer was printed on top of the LSM/YSZ interlayer using a single atomizer. The thickness of the LSM/YSZ interlayer was 41-44 microns. The smallest thickness obtained in the LSM cathode layer was approximately 35 microns. The porosity and microstructure of the printed layers can be seen in the Figure 18.

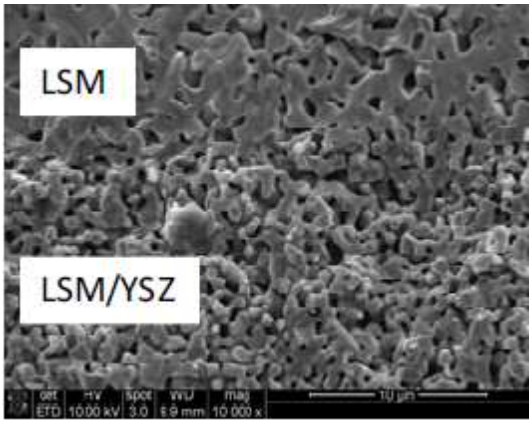

Figure 18: SEM of LSM/YSZ layer and LSM layer [Sukeshini et al., 2011]

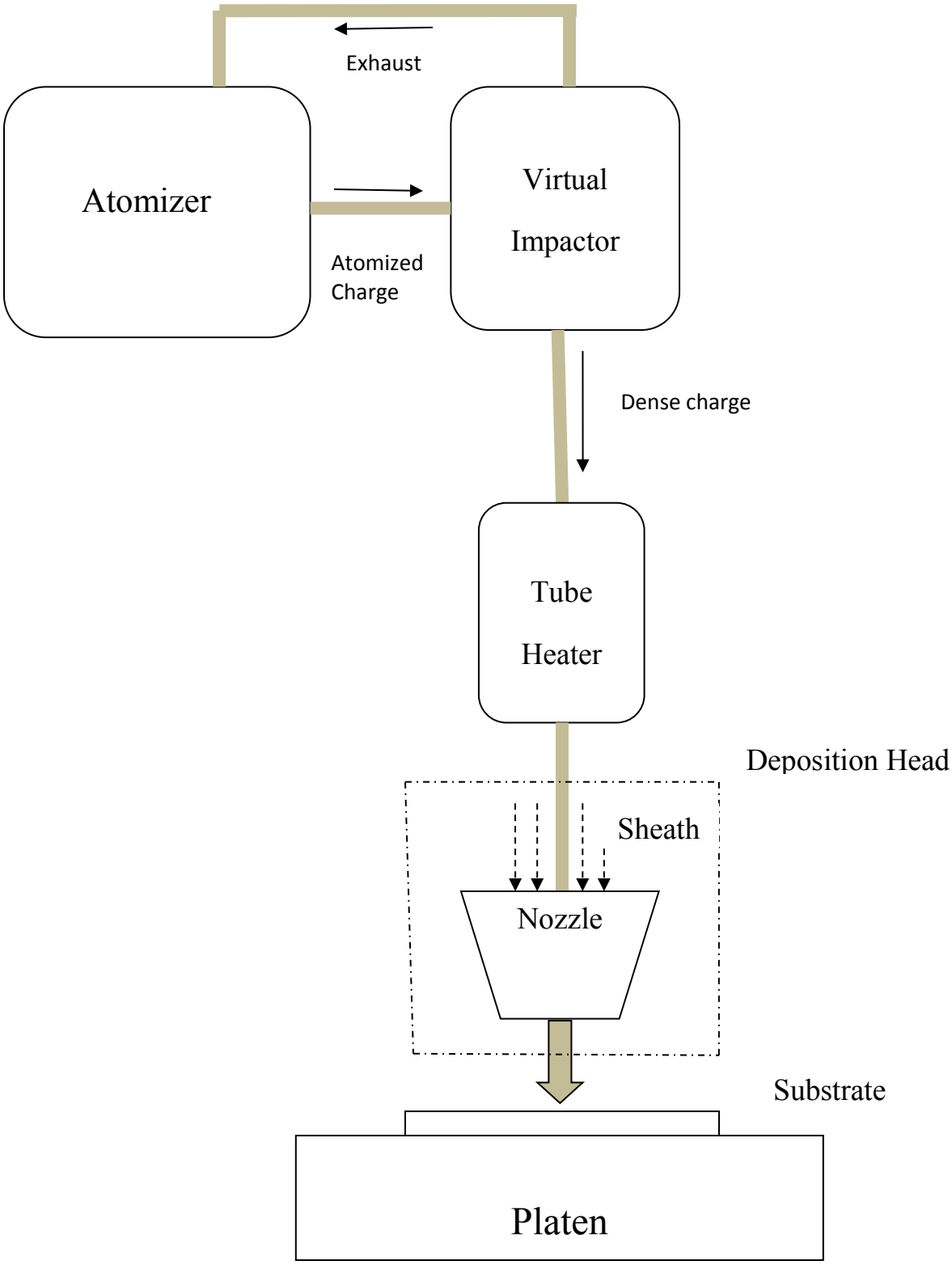

Figure 19: Schematic of aerosol jet Aerosol Jet printing system

With respect to Figure 19, the following process parameters can be adjusted to achieve the required feature properties:

1. Atomizer flow (ccm): Allows the carrier gas flow rate to be controlled through the atomizer unit. The passage of this carrier gas causes the ink in the atomizing cup to be atomized into a fine mist of sub-micron ink droplets.

2. Virtual impactor flow (ccm): Controls the flow rate of the impactor gas which bleeds off the excessive carrier gas in the aerosol stream. This densifies and controls the aerosol charge for its passage through the nozzle.

3. Sheath gas flow (ccm): Controls the flow rate of the collimating gas, which avoids any settling of aerosol droplets on the nozzle periphery. It also focuses the aerosol further to control the width of the resulting stream.

4. Platen temperature (^{o}C): Allows control of the platen temperature upon which the substrate rests. The platen can be heated to decrease ink viscosity and/or to accelerate drying of the ink after deposition. The platen temperature can also be reduced to as low as -40^{o}C by connecting a thermoelectric cold plate to allow freezing of the material.

5. Cup temperature (^{o}C): Allows control of the ink cup temperature. A higher cup temperature results in lower ink viscosity. It can also affect the size of the atomized droplets by altering the shear strength of the ink. Larger droplets with more liquid tend to flow out on the substrate (e.g. wider traces), whereas larger droplets with relatively low liquid content allow for rapid build-up of taller traces. Smaller droplet sizes can be challenging, because their low mass allows them to get carried outward with the exhaust gas as it impacts the substrate. The result is overspray or satellites in the printed lines.

6. Tube temperature (^{o}C): Controls the temperature of the tube through which the aerosol is transported to the deposition head. The variation in this temperature affects drying of the solvent in the aerosol, and hence the solid loading fraction in the droplets upon impact with the substrate.

7. Feed rate (mm/sec): Is the traveling speed of the platen in the X-Y plane. Its movement enables printing of various features on the substrate. The feed rate affects characteristics such as width, height and continuity of the printed feature.

8. Nozzle diameter (microns): Is the inner diameter of the nozzle opening through which the aerosol is focused onto the substrate.

9. Stand-off height (mm): Is the perpendicular distance between the nozzle and the platen. At different standoff heights, the velocity of the aerosol upon impact with the substrate changes. This result in different feature characteristics at different stand-offs.

The mentioned parameters affect the characteristics of the material carried in the aerosol, and hence the printed track. The particle physics and the aerodynamics of the aerosol and the printed layer also affect the feature characteristics. The possible outcomes also depend significantly on these conditions, and hence can even bear opposite outcomes for a particular parameter combination. Some possible print scenario outcomes are mentioned below.

Table 2: Possible outcomes of Aerosol Jet printing

Printed Feature	Description
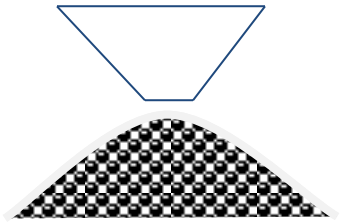	When the flow rates are high, feed rate is low or the material is still liquid, it tends to spread out on the substrate.
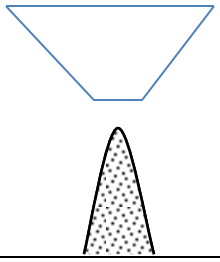	When material in the aerosol is dried up, it tends to stack up immediately on the substrate.
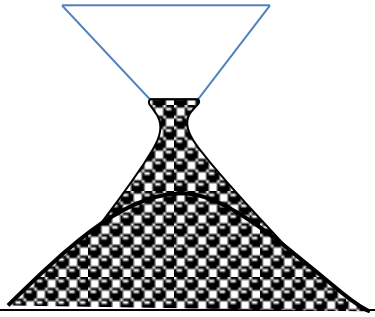	Though some features tend to spread on the substrate after printing, sometimes they provide a flat surface for the successive particles to stack up.
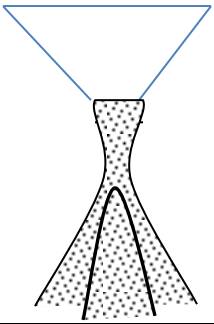	Though some features stack up immediately on the substrate, inertia of the droplets contained in the aerosol can produce over spray.

2.2. Characterization and Preliminary Experiments

The direct write process used in this study is an Optomec Aerosol Jet printing system. The first objective is to determine how the various process parameters affect the feature characteristics of the printed output. A preliminary experiment was therefore carried out to learn more about the Aerosol Jet printing process.

For preliminary experimentation, tracks were printed using the Optomec Aerosol Jet system under different parameter combinations. For the experiment, Yttrium Stabilized Zirconia (YSZ) powder from Fuel Cell Materials was used to prepare the ink. The powder was ball milled and then fired in a furnace at 100^{o}C for one hour with a 10 degree/min ramp rate. Ethylene glycol (Alfa Aesar) was used as the ink vehicle. A solid loading fraction of 30 vol.% was used for ink preparation. The ink was then mixed in a Thinky mixer for six minutes at 6000 rpm.

For the preliminary experiment, six parameters were kept constant while the other two were varied at two different values. Four samples were printed for each process setting. The first sample was produced with a single pass, and the others were produced with three, six and nine passes respectively. The parameter settings were set as follows:

Virtual impactor flow rate: 950 ccm

Sheath flow rate: 55 ccm

Platen temperature: 60^{o}C

Tube temperature: 80^{o}C

Cup temperature: Room temperature

Nozzle size: 250 microns

An experiment was set up with two factors and two levels. The factors of atomizer flow rate and feed rate were varied at two different settings as shown in Table 3.

Table 3: Parameter combination for preliminary experiment

Run Order	Feed rate (mm/s)	Atomizer flow rate (ccm)
1	15	1000
2	5	1150
3	5	1000
4	15	1150

The printed tracks were observed under a microscope, and their width was measured. Using the output data from the experiment, graphs were plotted for the width vs. the respective variable parameter. The data obtained is presented in Figures 20 and 21.

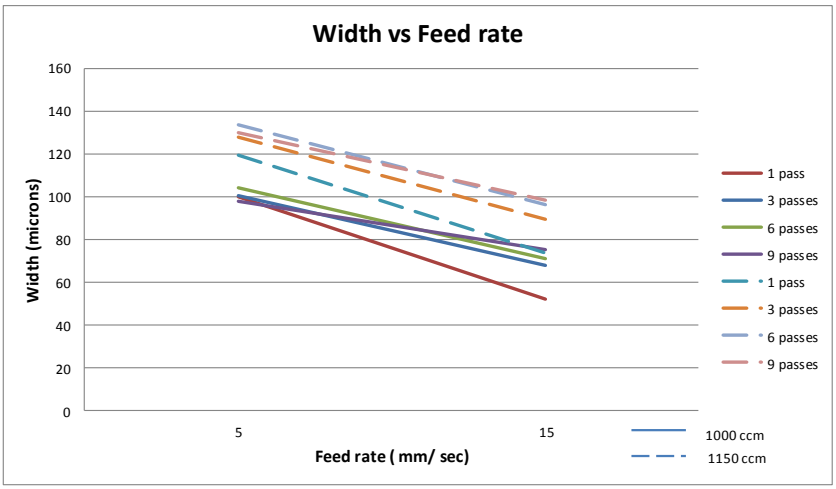

Figure 20: Width vs. Feed rate

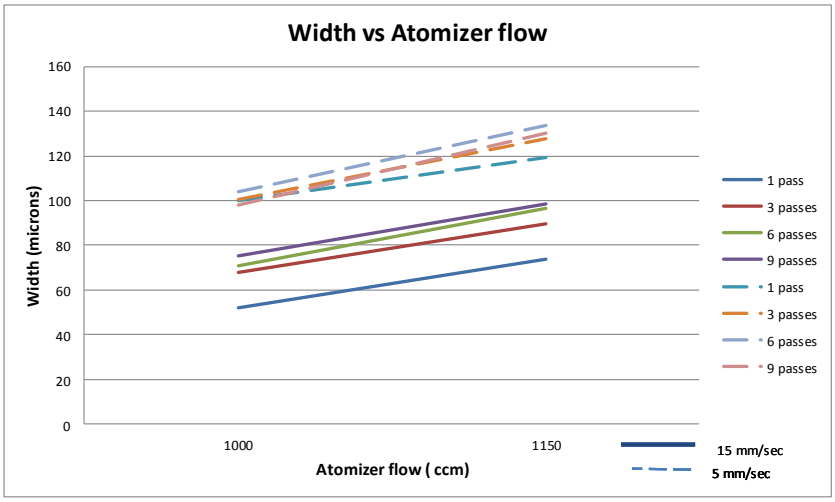

Figure 21: Width vs. Atomizer flow rate

Some observations from the data can be made as follows:

Feed rate: As we increase the feed rate, the deposited material does not have enough time to accumulate and spread out. At higher feed rates, we therefore expect lower line widths.

Atomizer flow rate: As atomizer flow rate increases, the amount of aerosol generated increases. We will therefore observe more material per pass assuming a constant impactor flow rate. We thus expect higher line widths at higher flow rates.

Number of passes: We also expect the line width to increase with the number of passes. This is observed due to the overspray of the material over previously printed layer.

We observe through our results similar effects of the process parameters on the response variable of line width. A clear distinction can be seen in the widths of tracks printed at two different feed rates. Higher width is observed at the low value of the feed rate. Also higher width is seen at the higher value of the atomizer flow rate, as expected. With each increasing pass, the width tends to increase. When we move from a single pass track to a multiple pass, a large increase in width is seen due to the expected overspray. With every subsequent pass, the increase in the width is minimal. Thus, we successfully demonstrate that change in the printing parameter affects the characteristics of a printed feature.

2.3. Ink Preparation and Viscosity Measurement

For ink preparation, the required quantity of samarium-doped ceria (SDC20-M) powder from Fuel Cell Materials (www.fuelcellmaterials.com) was measured. The powder was then mixed with the ink vehicle (ethylene glycol) in predetermined proportions. Sodium dodecyl sulfate (SDS) (Alfa Aesar) was added as a surfactant to the ink mixture. This mixture was then transferred to a planetary centrifugal mixer, a Thinky 310 mixer. It allows for simultaneous mixing and dispersion of included materials. The mixture was rotated for 6 minutes at 2000 rpm. Then the ink was transferred to the atomizing cup for printing.

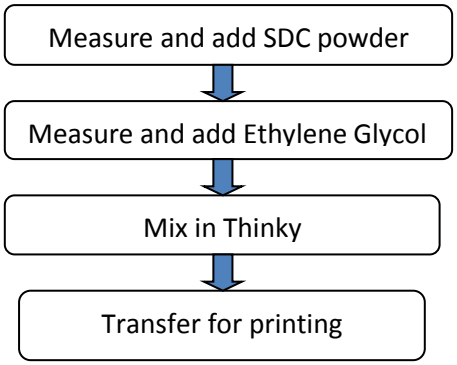

Figure 22: Ink preparation steps

The rheology of the ink used for printing is affected by the material used, the solid loading fraction, the ink vehicle used, additives used, etc. The same ink formulation was therefore used for all the experiments carried out in the study. The formulation used is provided in Table 4.

Table 4: Ink formulation table

Constituents for ink	Vol. %
SDC20-M	30
Ethylene Glycol	68
SDS	2

The ink properties are not found to remain constant over time. This is a result of the volatility of the constituents used in the ink mixture. The obvious challenge is that the process output can drift over time, even when the same printing parameters are used. An important rheological behavior of inks is whether they are Newtonian or Non-Newtonian. Newtonian inks have constant viscosity at different shear rates. The viscosity of Non-Newtonian inks varies at different shear rates. The viscosity of a liquid can be measured as a function of shear rates using a viscometer. The plot of viscosity vs. shear rate helps with understanding the behavior of the ink.

For this study, a Brookfield DV-E viscometer was used to measure viscosity as a function of spindle speed. Spindle S61 was used for the experiment that has a viscosity measurement range of 15cP to 20,000cP. Spindle speed is a direct indicator of shear rate for a given spindle diameter. Figure 23 plots viscosity versus spindle speed for the SDC ink used in this study. The SDC ink used in the study possesses shear-thinning behavior. This means the SDC ink's viscosity decreases as the shear rate applied increases.

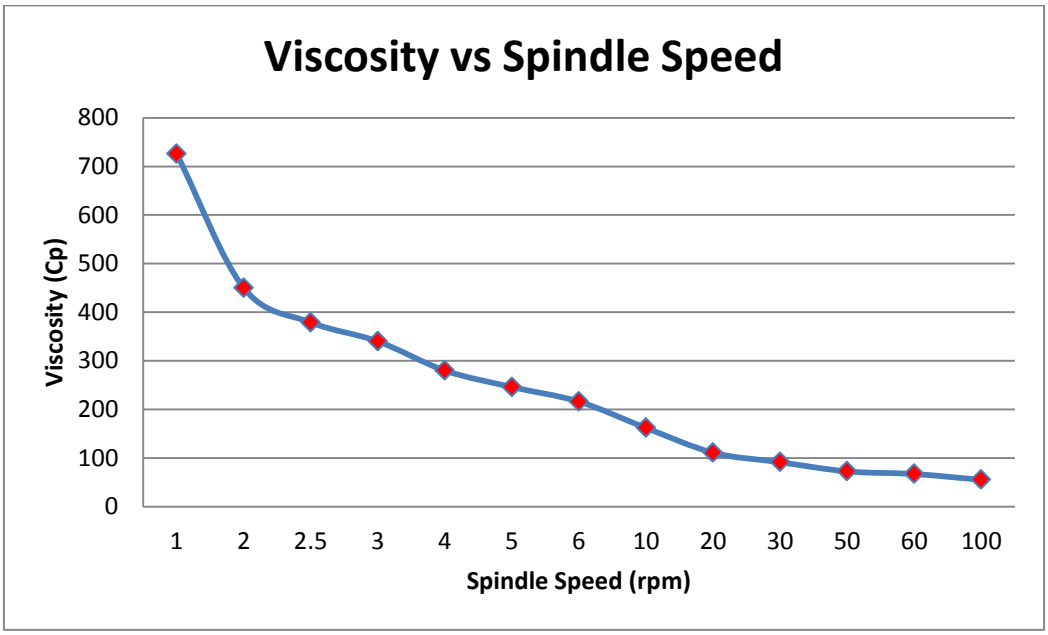

Figure 23: Viscosity vs. Spindle speed

2.4. Screening Experiments

This research is aimed at understanding the effects of Aerosol Jet process parameters on the process output. We initially used a screening experiment to identify factors that have a significant effect on the response variables of interest. For this research the seven process parameters discussed above were selected for study. It was decided to use a 2^{7-3} fractional factorial model of resolution IV because using a full factorial model with 7 factors would result in large number of runs. We use a fractional factorial model which minimizes the number of runs and allows saving on resources used for experimentation. This result was 16 unique parameter combinations. In addition, it was decided that 3 samples would be printed for each combination. The average of these three samples was taken as the final value while carrying out measurements to minimize random variations. This resulted in 48 total runs. As no replicates were considered the error was estimated by using the three way and higher order interactions. All runs were randomized to minimize the effect of uncontrollable variables.

2.4.1. Selection of Parameter Values

For all experiments, a 300 micron nozzle size was used. This was done as the possible range of output feature resolution that can be obtained using this size is enough for the application in hand. In addition, a parameter for the difference in flow rates between the atomizer and virtual impactor (FR_Δ) was used while selecting values for factor levels. This was done because VI flow rate only makes a difference when considered with atomizer flow rate. As the difference between these flow rates is what that affects the output net flow rate. In addition, for the machine to continue printing a feature, the atomizer flow rate (FR_A) has to be greater than the virtual impactor flow rate (FR_{VI}). If one were to randomly choose sheath (FR_S), atomizer (FR_A) and VI (FR_{VI}) flow rate values, there would be some parameter combinations that could result in no output. Considering delta flow rate (FR_Δ) as the process parameter, we can circumvent these constraints. Now the total process flow (F_T) can be represented as,

$$F_T = (FR_A - FR_{VI}) + FR_S \quad \text{(Eq. 1)}$$

Considering this process understanding, the delta flow rate is defined as the difference between atomizer flow rate and virtual impactor flow rate set in the system.

$$FR_\Delta \text{ (ccm)} = FR_A \text{ (ccm)} - FR_{VI} \text{ (ccm)} \quad \text{(Eq. 2)}$$

Printing feasibility tests were conducted to determine ranges of process parameter values that produced continuous lines without excessive over spray. For the lines to be continuous and well defined, an appropriate tube heater temperature must be maintained. This is required so that the ink is sufficiently dry to form a line that does not flow or excessively spread on the substrate upon printing. Polyethylene tubing was used for all experiments, and the maximum possible tube temperature that can be used without melting the tube is 90°C. For finding the upper range of atomizer flow, the maximum possible flow rate value at which printing can be done was

determined at a tube temperature of 90°C. At an atomizer flow of 920 ccm, lines were printed without clogging the system for 60 continuous minutes. An atomizer flow of 520 ccm marked the low level at which the SDC ink started atomizing in the cup. An upper limit of 80°C was set for platen temperature. Beyond this temperature, the Mylar substrate used for the experiments warped. The lower levels of tube and platen temperatures were determined by observing the lowest temperatures at which the ink printed a well-defined line instead of spreading on the substrate. The selected parameter values are shown in Table 5.

To determine whether lines were well-defined or not, the output lines during the feasibility trials were qualitatively checked for errors of overspray, satellites, bulging, and line edge definition. Figure 24 shows examples of well-defined and poorly defined lines. All samples were printed using the Optomec Aerosol Jet process. After printing, the samples were air dried for 24 hours before width and height measurements were taken.

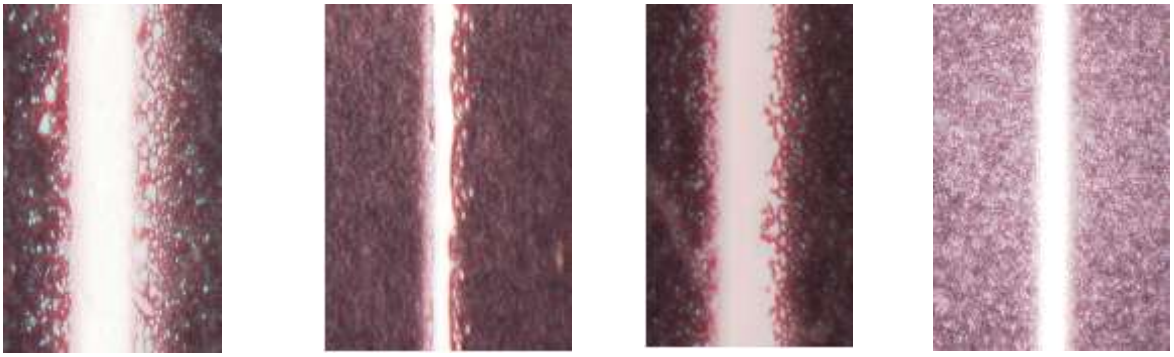

a. Satellites **b. Bulging** **c. Poor edge definition** **d. well- defined**

Figure 24: Line quality

Table 5: Screening process parameter levels

Factor	Name	Low	High
A	Atomizer flow rate	520	920
B	Delta	20	60
C	Cup temperature	30	40
D	Platen temperature	40	80
E	Feed Rate	2	14
F	Tube temperature	40	90
G	Sheath flow rate	80	150

2.4.2. Width Measurement

The width of the printed lines was measured using a Hirox KH-7700 digital microscope. The line width was measured using 2D measurement tools on the microscope. Single layer prints are often a few microns thick, and it is sometimes difficult to differentiate between the printed line

and the over spray which surrounds the line. This may lead to over estimation of the line width. Hence, three layers were printed for each parameter combination in order to form a clearly distinct line that could be measured using the microscope.

2.4.3. Height Measurement

The height of the printed lines was measured using a Keyence IL-030 laser profilometer. The Profilometer consists of a multi-function analog laser sensor, an amplification unit, and a communication unit. For measuring the height, the laser was focused on the substrate upon which lines were printed. This substrate was set as the reference. Then the beam was positioned on the printed surface to measure its height with respect to the substrate. For each height measurement, 2mm × 2mm squares were printed on die pressed YSZ disks. The laser beam was rastered over a distance of 1 mm, and a reading was taken every 10 microns. An average of the collected data points measured over the surface of the square sample was taken as the height measure for the sample.

2.4.4. Result and Analysis

The results of the fractional factorial experiment were analyzed using Minitab. The response variables of width and height were analyzed separately, as the significant parameters affecting these variables were expected to be different for each of these responses based on earlier lab experiments. For analysis, the response variable of height was transformed to square root of height. This transformation was done since the residuals for the non-transformed height response did not satisfy the normality assumption. Half normal plots were generated for the response variables. For SQRT height, referring to the half normal plots, the atomizer flow rate (A), feed rate (E), tube temperature (F) and interaction of atomizer flow rate & feed rate (AE) were identified as the significant factors affecting the response height (refer to appendix B1). For width, referring to the half normal plots, delta (B), feed rate (E) and sheath flow rate (G) were identified as the significant factors affecting the response width (refer to appendix B2).

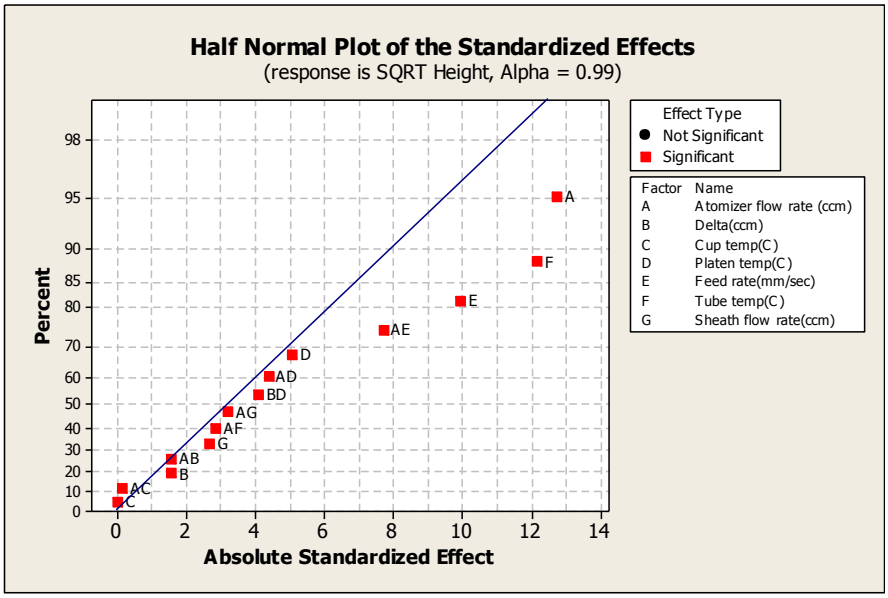

Figure 25: Half normal plots for SQRT height

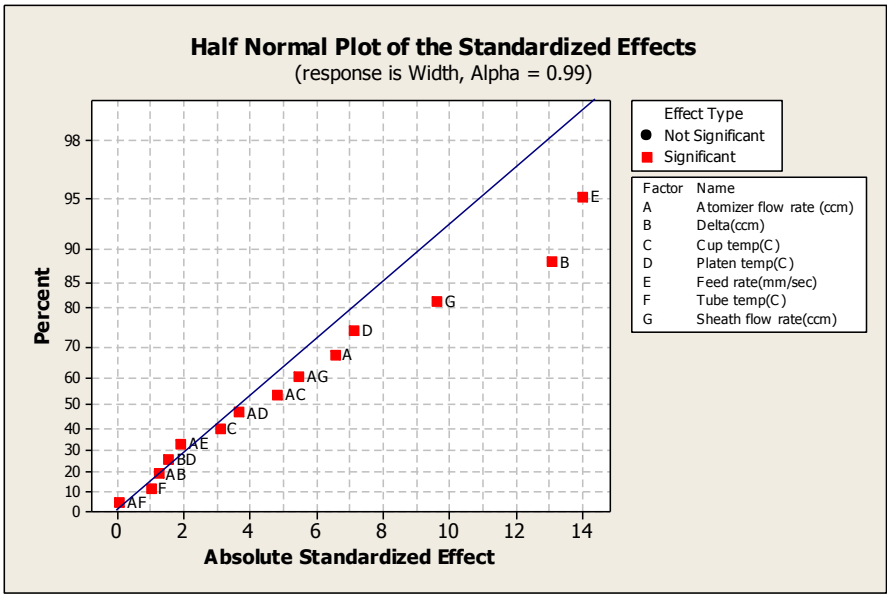

Figure 26: Half normal plots for width

Residuals were plotted by selecting the significant factors for both the response variables. From the residuals, (refer to appendix C1 & C2) it can be inferred from the normality probability plot that the normal distribution assumption cannot be rejected. Furthermore, the residuals vs. fits and residuals vs. order show no pattern or trend. A regression equation was therefore fitted to the reduced models in Minitab. Regression equations Eq. 3 and Eq. 4 describe responses for height and width respectively.

SQRT (height) = 3.24622 + 0.621564×A + 0.593189×F - 0.48488×E - 0.376019×AE ……. …… (Eq. 3)

Width = 99.6437 + 11.8688×B - 12.6937×E - 8.71875×G ……...(Eq. 4)

2.4.5. Validation

Using the regression equations from Minitab, one can attempt to predict response values for selected process parameter settings. This is done to check validity of the model that is being fit to the data.

Table 6: Screening experiment levels for height

	Atomizer flow rate (ccm)	Tube temp (˚C)	Feed rate (mm/s)
Low (-)	520	40	2
High (+)	920	90	14

Table 7: Screening experiment levels for width

	Delta (ccm)	Sheath flow rate (ccm)	Feed rate (mm/s)
Low (-)	20	80	2
High (+)	60	150	14

For verification runs, center point values and values which were previously not considered in the screening experiment (Tables 6 & 7) were taken as the process parameter values, forming three process combinations (Tables 8 & 9). This was done to check for any possible curvature in the data. The encoded values for the parameters in verification runs were calculated using the following equation [Parody, 2011],

$$X_i = \frac{\xi_i - \left(\xi_{low} + \xi_{high}\right)/2}{\left(\xi_{high} - \xi_{low}\right)/2} \qquad \text{---------- (Eq. 5)}$$

where,

ξ_i = Parameter value in natural unit

X_i =Parameter value in coded unit

Table 8: Validation experiment data tables for height

Process combination	Atomizer flow rate (ccm)		Tube temperature (C)		Feed rate (mm/sec)	
	Coded	Actual	Coded	Actual	Coded	Actual
1	-0.5	620	-0.5	52.5	-0.5	5
2	0	720	0	65	0	8
3	0.5	820	0.5	77.5	0.5	11

Table 9: Validation experiment data tables for width

Process combination	Sheath flow rate (ccm)		Delta (ccm)		Feed rate (mm/sec)	
	Coded	Actual	Coded	Actual	Coded	Actual
1	-0.5	97.5	-0.5	30	-0.5	5
2	0	115	0	40	0	8
3	0.5	132.5	0.5	50	0.5	11

For the height validation, two samples were printed for each parameter combination. Squares with dimensions of 2 mm × 2 mm were printed on die pressed YSZ discs. Height measurements were taken with the Keyence laser profilometer. The actual height values from the experiment are documented in Table 10. These actual measured values (refer figure 27) are very close to the predicted values and fall within 2% of the predicted height values. The predicted values are also within the range of standard error (S) limits (refer appendix C1) for the reduced model. We

conclude that the model adequately predicts height of a printed sample within the parameter value ranges of the model.

Table 10: Height validation predicted vs. actual

Process combination	Predicted(um)	Actual (um)	
		Sample 1	Sample 2
1	7.768	7.68	7.6
2	10.537	10.71	10.82
3	12.37	12.31	12.28

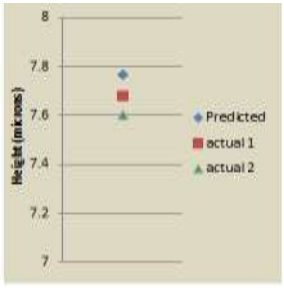

Process combination 1

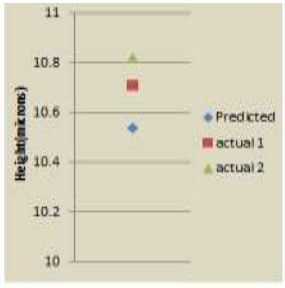

Process combination 2

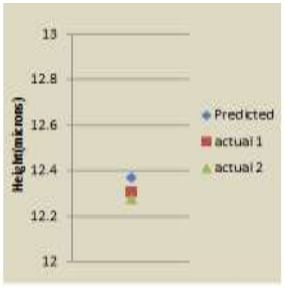

Process combination 3

Figure 27: Predicted vs. actual height

For width validation, two lines were printed on Mylar substrate for each parameter combination. The widths were measured using the 2D measurement tool on the Hirox microscope. The actual measured width values are noted in Table 11. There is a significant deviation observed between the actual measured values and predicted width values (refer figure 38). This was observed as the ethylene glycol in the ink balls up given enough time to rest. Hence validation samples that were measured after 24 hours measure significantly less than the predicted values where some measurements were taken immediately after the experiment was done.

Table 11: Width validation predicted vs. actual

Process combination	Predicted(um)	Actual (um)	
		Sample 1	Sample 2
1	104.415	100.2	99.8
2	99.643	94.8	95.2
3	94.871	91.6	92.7

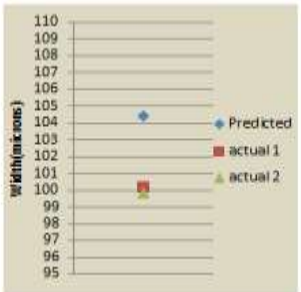

Process combination 1

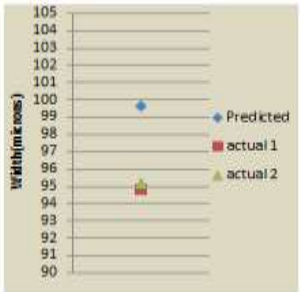

Process combination 2

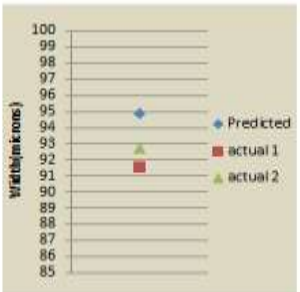

Process combination 3

Figure 28: Predicted vs. actual width

2.5. Higher Order Model

For the response of width, the R-squared value of 49.95 % (refer to appendix C2) for the reduced model is not satisfactory. This means that only 50% of the response variable (width) variation is explained by its relationship with the process parameters. In addition, a clear trend was observed in the residuals vs. observation order plots (refer to appendix C2). The reason for this was believed to be the non- uniform drying time of width samples. To ascertain whether or not lack of curvature exists within the feasible process parameter range (design space), a higher order model was designed for the width response. We consider three factor levels for the factors of sheath flow rate, delta and feed rate that affect the width of a printed track. The process parameter levels used for the experiment are shown in Table 12. A 3^3 full factorial experiment was designed. All runs were randomized to minimize the effect of uncontrollable variables. During printing, atomizer flow rate was set to 920ccm. The tube, platen, and cup temperatures were maintained at 90^{o}C, 80^{o}C, and 40^{o}C respectively. The line width was measured after samples were uniformly air dried for 24 hours.

Table 12: Higher order model process parameter values

	Delta (ccm)	Sheath flow rate (ccm)	Feed rate (mm/s)
Low -	20	80	2
medium	40	115	8
High +	60	150	14

2.5.1. Results and Analysis

To analyze the results of the full factorial model, the ANOVA function in Minitab was used. All the main factors including the two way interaction effects were considered for the best fitting regression analysis. Referring to the ANOVA table, active interaction effects between the significant parameters were identified by referring to the calculated p-values (refer to appendix C3). This model predicts the response through the significant factors of sheath flow rate (G), delta (B), feed rate (E) and interaction effects of sheath & delta (BG) and square of feed rate (E^2). The remaining terms were used to estimate the model experimental error. This reduced regression model was then fitted to our data. From the generated residuals, (refer to appendix C4) we can conclude from the normality probability plot and the normality test for residuals that the residuals come from a normal distribution. Furthermore, the residuals vs. fits and residuals vs. order plots show no pattern. So based on the residual analysis, the model seems adequate. A regression equation was therefore fitted to the experimental data. The regression equation for the fitted model is,

$$\text{Width} = 94.9778 - 9.27222\times E - 8.97222\times G + 10.7444\times B + 4.19167\times BG + 4.22778\times E^2 \quad \text{…….. (Eq. 6)}$$

2.5.2. Validation

Using this regression equation from Minitab, the width response was predicted for selected values of the significant process parameters. The same center values for significant process parameters used earlier were used in this validation. Encoded values were determined by referring to Equation 5. Predicted values for width were calculated by substituting encoded values in the regression Equation 6. Comparison of actual width values to the predicted values of width is documented in Table 13. The actual values are within +/-2% of the predicted width values.

Table 13: Final model predicted vs. actual

Process combination	Predicted(um)	Actual (um)	
		Sample 1	Sample 2
1	100.8322	100.2	99.8
2	94.97778	94.8	95.2
3	93.33222	91.6	92.7

The higher order model predicts the widths for a printed track more accurately as compared to the earlier screening model. The standard error of 14 from the screening experiment goes down to 5 in the higher order model. Furthermore, the R-squared value increases from the 49.5% to 84% in the higher order model. Figure 29 shows the difference between screening and final experiment predictions as compared with the actual values.

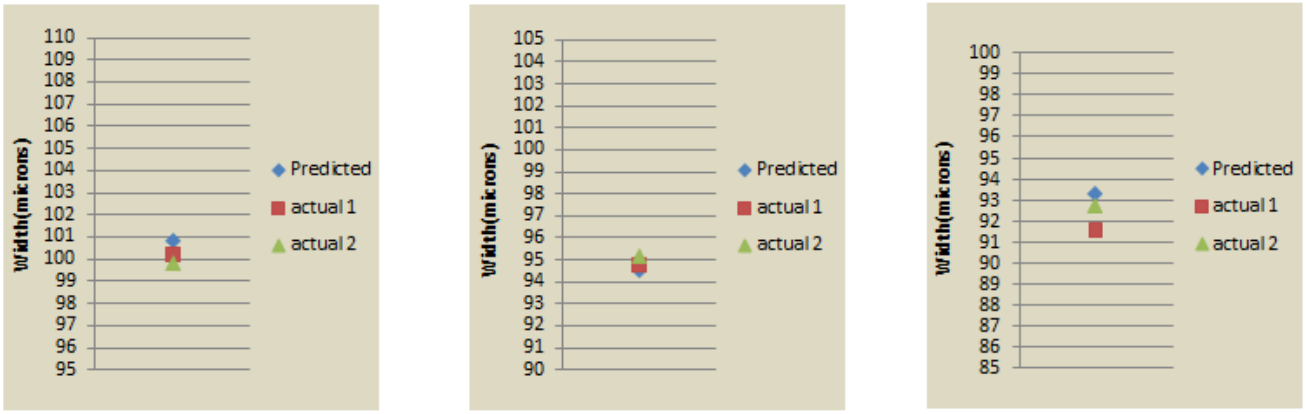

Process combination 1 | Process combination 2 | Process combination 3

Figure 29: Final predicted vs. actual width

2.6. Discussion of Results

From the experiments carried out, it is observed that process parameters of atomizer flow rate, feed rate, and tube temperature significantly affect the height of the printed track. From the experimental analysis, it is seen that high values of atomizer flow rate and the tube temperature are helpful in building height. The highest levels of atomizer flow rate and tube temperature that aided in stacking of SDC without clogging the system were observed at 920 ccm and 90^{o}C respectively. Though higher levels enable stacking, excessively high values can actually reduce the aerosol flow due to clogging. If tube temperature is increased further, it may dry the ink before it exits the nozzle. It can also melt the feed tube and hence clog the system. The feed rate of the platen also affects the stacking up of material on the substrate. At lower feed rates with suitable ink temperatures, the ink stacks up a significant amount to build up height. This lower value of the feed rate in the experiment was 2 mm/sec. This ensured stacking up of SDC at a tube temperature of 90^{o}C.

The factors that significantly affected the width of a printed track were delta, sheath flow rate and feed rate. From the analysis of experimental results, we can infer that narrow lines were obtained with a low value of delta (i.e. at high virtual impactor flow rates). Increasing the virtual impactor flow rate bleeds off the carrier gas and fine ink droplets in the aerosol hence making the aerosol stream dense and narrow. Increasing the sheath flow rate further focuses the aerosol stream through the nozzle, reducing the width of the printed track. The high sheath flow rate of 150 ccm was used in the experiment. When ink temperatures are low (i.e. less drying of the ink before deposition), lower feed rates cause ink to flow out and spread instead of stacking up as in the case of elevated temperatures. This caused high width at lower feed rates during experimentation.

It is possible to combine lessons learned from this experimentation for purposes of printing high aspect ratio HeteroFoam structures. Namely, one can restrict the flow rate to ensure moderate amounts of ink atomization (i.e. do not flood the nozzle with ink). High ink temperatures and low feed rates will enable immediate stacking of this atomized material as it is deposited on the substrate. This will result in thin, but tall, structures.

If one desires uniformly deposited films, then low temperatures and low feed rate help ensure spreading of the ink on each printing pass. High flow rates can be used to scale the amount of material deposited per pass to fabricate a thick film of required height.

2.7. High Aspect Ratio Structures

In this section, lessons learned from the process parameter modeling work are applied in the fabrication of structured SDC pillar arrays. Lejeune et al. (2009) used ink jet processing to print high aspect ratio micro pillar arrays. The authors used drop on demand and multi nozzle piezoelectric inkjet print heads to produce micro pillar arrays. The system was used to stack micro-droplets in order to build 3D pillar structures. For achieving the desired feature sizes, the aperture of the printing head and the spreading of the droplets were controlled. The characteristics of the printed features were thus controlled by the driving parameters of the print head. In the study, different ink formulations with varying percentages of ceramic loading and binder weight were first tested using a single nozzle to print successive layers. The greatest stacking was observed with highest ceramic loading and highest binder weight. This formulation also resulted in quick drying of the ink before deposition of the second layer. The multiple nozzle system was then used to simultaneously print multiple droplets. The delay in printing the second successive layer was adjusted as per the drying time required. This was done repeatedly for layer by layer fabrication of a micro pillar ceramic array. The PZT micro-pillar array embedded in a polymer matrix was fabricated for its application in medical imaging probes as seen in Figure 30.

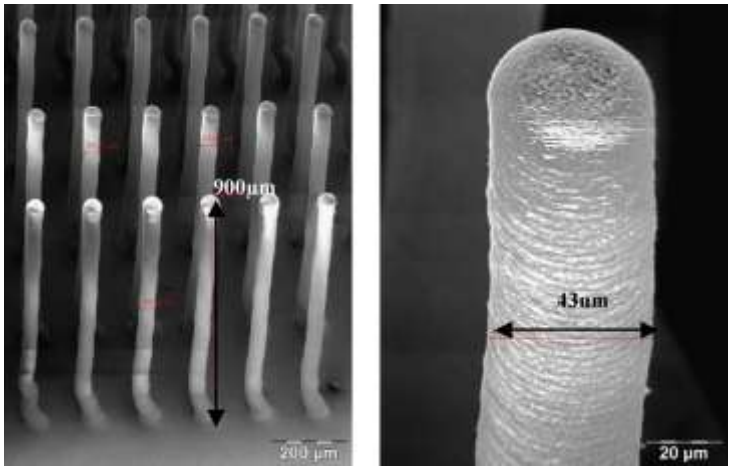

Figure 30: SEM of PZT micro pillar array [Lejeune et al, 2009]

Machining process such as micro wire-EDM has also been used to fabricate high aspect ratio micro pillar arrays. Chuang et al. (2005) developed a method of 'reverse wire EDM' to fabricate these high aspect ratio structures. They used a system where a micro-wire EDM was mounted on a turn table, and a work piece was held in a micro chuck spindle. The machining was done by moving a 20 micron thick wire located below the surface of the work piece. Using this technique, a 10×10 micro pillar array, as shown in Figure31 was fabricated in which the width and height of each pillar was 21 and 700 microns respectively. The authors discuss potential applications of such micro electrode arrays in batch production of micro holes in micro EDM (Chuang et al, 2005). They also have uses in the fabrication of micro medical devices to sense nerve signals and

other biological sensing applications. However, the application of this process is limited to electrically conductive materials.

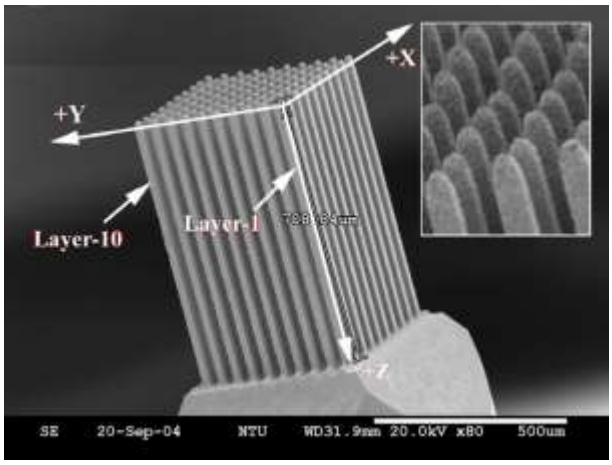

Figure 31: SEM micrograph of a wire-EDM micro pillar array structure [Chuang et al, 2005]

Lithographic processing methods can also be used to fabricate high aspect ratio micro structures including pillar arrays. Advanced lithographic techniques are used for layer by layer coating and exposure to generate high aspect ratio structures such as micro pillars. In such applications, resist materials are required to have stringent capabilities as the aspect ratio gets higher (Campo and Arzt, 2008). In this study, PMMA pillar arrays with an aspect ratio of 10 were obtained by vertical and tilted x-ray exposure as shown in Figure 32

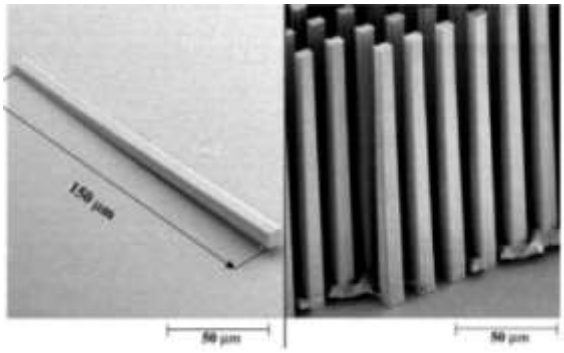

Figure 32: PMMA micro pillar arrays by inclined lithography [Campo & Arzt, 2008]

Selection of an applicable process to fabricate micro-pillar arrays is driven by the feature characteristic requirements for these arrays. The selected process limits the possible materials to be used and the possible dimensions of the printed structures. Some challenges that the previous studies discuss while fabricating these pillar arrays include:

1. Getting the micro pillars closely packed to produce higher pillar density per given area.
2. Fabricating features with multiple materials and graded materials.

Using multiple materials and grading the composition of these materials on the fly while printing such structures is a considerable limitation when one considers the processes mentioned in this study. It is also important to consider densely packing these pillars together to achieve higher surface area for certain applications. To further build upon the mentioned studies, these areas need to be addressed while fabricating such micro-pillar arrays.

2.7.1. Procedure

To print micro pillar arrays using the Aerosol Jet process, appropriate flow rates that allow stacking up of ink must be identified to build a significant height. The flow rates have to be just high enough to atomize the ink without excessive ink flow, the tube temperature must be high enough so that the ink dries enough to stack up on the substrate, and the platen temperature has to be high enough so that the ink stacks up immediately as it lands on the substrate without flowing out. SDC ink was used for this experiment. A higher solid loading of 34% vol. was selected to aid in stacking of the material.

Table 14: Pillar array ink formulation table

Constituents for ink	Vol. %
SDC20-M	34
Ethylene Glycol	64
SDS	2

For printing the micro pillar arrays, we use the high value of tube temperature for increased height and low values for atomizer flow rate, delta and sheath flow rate were selected as explained in the result discussion earlier in the study. The platen temperature was kept at the high value, as we want the material to dry as soon as it hits the substrate so that it stacks up immediately. The process parameter values used for printing pillar arrays were kept constant at the levels shown in Table 15.

Table 15: Constant parameters values

No	Process Parameters	Levels
1	Atomizer flow rate(ccm)	520
2	Delta(ccm)	20
3	Cup temperature(˚C)	30
4	Platen temperature(˚C)	80
6	Tube temperature(˚C)	90
7	Sheath flow rate(ccm)	80
8	Nozzle diameter(um)	300

After narrowing on the process parameters, a program (tool path) for the Optomec machine was developed to print the pillar grid, (refer appendix D1). The program commands the nozzle to wait in a position for a pre-calculated amount of wait time until a pillar is formed from the deposited material of a required height. After the prescribed amount of time, aerosol flow to the nozzle is shut off, thus stopping material deposition on the substrate. The nozzle is indexed to a new position, and flow is restored for the prescribed amount of time to print the next pillar. To calculate the wait time, studies were done to note the time required in seconds to stack the material for a required height subject to the constraint that the printed pillar doesn't collapse or blow over. Using process parameters from Table 15, printing for 4 seconds produced pillars that were approximately 450 microns tall. This was done repeatedly in multiple locations to form an 8×8 grid of SDC pillars.

While printing, it was sometimes observed that the exhaust stream produced while printing one pillar would blow over an adjacent previously printed pillar. To circumvent this issue, the program was modified so that alternate pillar columns would first be printed in the array. Then to complete the array, the remaining columns in between the previously printed ones were printed. Doing this gave enough time for pillars to dry before an adjacent pillar was printed. The added green strength allowed pillars to remain intact during printing. The average heights of pillars and the distance between pillars in a grid were measured. The results for this experiment are documented in Table 16. The heights of 4 pillars within an array were measured, and the average height value was taken as the height value for the array. The height was measured using the multi-focus synthesis tool on the Hirox microscope. For measuring the distance between pillars in an array, the distance was measured from the top view of the array using the 2D measuring tool in the Hirox microscope. The distance between pillars was measured for four different values within a array, and the average value was taken as the distance between pillars value for the array.

Table 16: Pillar array experiment table

Sample Arrays	Stand-off distance(mm)	Distance between pillars (um)	Height (um)
1	3	123.61	463.2
2	3	120.56	458.7
3	3	127.18	458.4
4	10	45.43	432.8
5	10	40.21	450
6	10	52.323	458.2

To build upon the previous studies, an attempt was made to reduce the distance between adjacent pillars. This allows one to pack more pillars within an array of same given dimension, hence significantly increasing the total surface area for the array. During previous experiments, the challenge was that pillars would blow away if the distance between two pillars was too small. In the second study, the standoff height of the nozzle above the substrate was modified. All other process parameters were kept constant. Similar 8 × 8 pillar arrays were printed using the increased standoff height. The average height of pillars and distance between pillars was measured by using Hirox microscope. Following are the microscope images for pillar arrays with two different standoff settings.

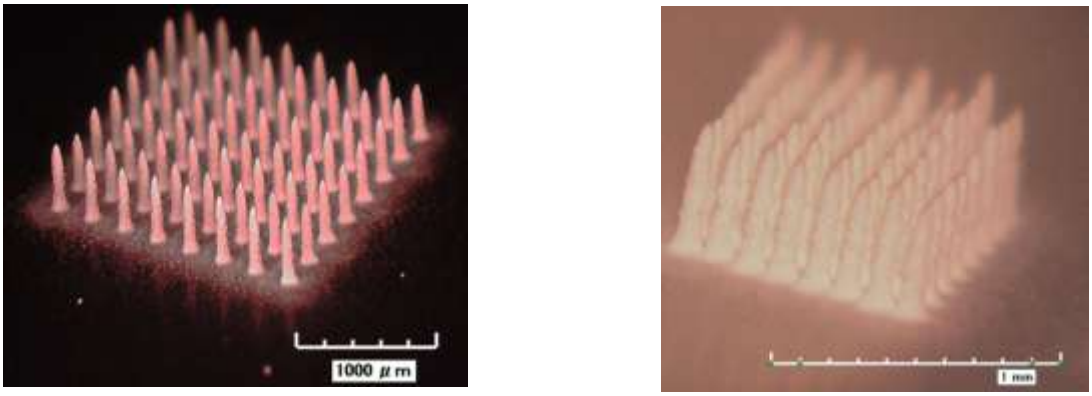

(a) (b)

Figure 33: Figure pillar array samples with (a) 3mm standoff and (b) 10 mm standoff

2.7.2. Results

High aspect ratio pillar arrays can be fabricated using the Aerosol Jet printing process. The average width of the obtained pillars was 60 microns, and the average height of the obtained pillars was approximately 450 microns. Pillars with aspect ratios of approximately 7.5 were successfully fabricated. During fabrication, it was found that low printing flow rates at which the ink just starts to atomize coupled with high tube and platen temperatures help dry the material as soon as it lands on the substrate and hence aids with stacking of the material. Furthermore, drying the material as soon as it lands on the substrate helps the printed feature to maintain its shape without collapsing or flowing outwards. The standoff distance between the nozzle and the substrate significantly affects how closely the pillars can be stacked in an array. The hypothesis is that the velocity of the sheath gas decreases as the distance from the nozzle increases. Thus the larger standoff distance produces a lower gas velocity, and hence pressure, acting upon previously printed pillars. When the standoff distance was increased to 10mm, pillar arrays with a gap of as low as 40 microns were obtained.

3. Conclusions and Future Work

3.1. Conclusions

An Aerosol Jet printable ink formulation for the SDC ink was prepared and used for all the experiments carried out in the study. Feasible parameter ranges were identified for all the variable process parameters to print a well-defined SDC feature. Through the screening experiments, the factors of atomizer flow rate (A), tube temperature (F), and feed rate (E) were found to most significantly affect the height of a printed track. In addition, the factors of sheath flow rate (G), delta (B), and feed rate were found to significantly affect the width of a printed track. A regression equation as mentioned below was generated from the experimental data to predict the square root of the height of a printed track.

$$\text{SQRT (height)} = 3.24622 + 0.621564\times A + 0.593189\times F - 0.48488\times E - 0.376019\times AE$$

The equation predicts height within a 2% variation as compared to the actual value, and it is also within the limits considering a standard error (S) of 0.5. For width, the R squared value of 49% for the screening model was found to be unsatisfactory also a clear trend was seen in the residuals vs. order plot. So a full factorial higher order model was designed for predicting width. A regression equation as given below was generated from the full factorial experimental data to predict width of a printed track.

$$\text{Width} = 94.9778 - 9.27222\times E - 8.97222\times G + 10.7444 \times B + 4.19167\ BG + 4.22778\times E^2$$

The equation predicts width of a printed track within a 2% variation as compared with the actual value and within the limits of standard error (S) of 5.09. The R squared error value for the model increased to 84%.

The ability to print high aspect ratio structures via the Aerosol Jet process was successfully demonstrated through fabrication of micro-pillar arrays. Aspect ratios up to 7.5 were successfully fabricated using the process. Through initial trials, appropriate parameter settings were found for the SDC ink to fabricate pillar arrays. It was found that an increase in the stand-off distance enabled a significant reduction in the distance between adjacent pillars.

3.2. Future Work

The results of this study have helped derive relationships between Aerosol Jet process output and the process parameters. This process knowledge can be used to fabricate HeteroFoams for various energy applications. This study is intended to aid in the selection of the appropriate process settings depending on intended feature characteristics of structured functional films.

In addition to the internal variable process parameters of the Aerosol Jet printing process, the effects of external factors such as ink formulation, substrate material, and post print treating must be studied. Solid loading in inks is also a crucial factor, as it affects the resulting porosity as well

as the microstructure of the printed features. It also affects the spreading or the stacking characteristics of the ink upon printing. The use of different solvents affects the printability and contributes to the feature characteristics. Ink formulations with high and low vapor pressure co-solvents have been printed with the Optomec Aerosol Jet system. The effect of varying proportions of these solvents must be studied on the response of width and height. Including the effects of these factors in addition to the factor effects concluded in this study would result in a more accurate model to predict the system response.

Further investigation needs to be done to study the effects of all the variable process parameters on the feature characteristics of a micro-pillar array. A parameter model can be built aimed at fabricating high aspect ratio and closely packed micro pillars. The Aerosol Jet system is also capable of co-atomizing two materials on the fly to fabricate material with functionally graded features. The use of co-atomization to fabricate graded pillar arrays is recommended for exploration.

Bibliography

Adler, S. B. (2004). Factors governing oxygen reduction in solid oxide fuel cell cathodes. Chemical reviews, 104(10), 4791-4844.

Boaro, M., Vohs, J. M., & Gorte, R. J. (2003). Synthesis of highly porous yttria-stabilized zirconia by tape-casting methods. Departmental Papers (CBE), 12.

Carrette, L., Friedrich, K. A., & Stimming, U. (2001). Fuel cells–fundamentals and applications. Fuel cells, 1(1), 5-39.

Chan, S. H., Khor, K. A., & Xia, Z. T. (2001). A complete polarization model of a solid oxide fuel cell and its sensitivity to the change of cell component thickness. Journal of Power Sources, 93(1-2), 130-140.

del Campo, A., & Arzt, E. (2008). Fabrication approaches for generating complex micro-and nanopatterns on polymeric surfaces. Chemical reviews, 108(3), 911.

Du, Y., Sammes, N., & Tompsett, G. (2000). Optimisation parameters for the extrusion of thin YSZ tubes for SOFC electrolytes. Journal of the European Ceramic Society, 20(7), 959-965.

Etsell, T. H., & Flengas, S. N. (1970). Electrical properties of solid oxide electrolytes. Chemical Reviews, 70(3), 339-376.

Fleig, J. (2003). Solid oxide fuel cell cathodes: polarization mechanisms and modeling of the electrochemical performance. Annual Review of Materials Research, 33(1), 361-382.

Flesner, R. (2009). Modeling of Solid Oxide Fuel Cell functionally graded electrodes and a feasibility study of fabrication techniques for functionally graded electrodes.

Gibson, I., Rosen, D. W., & Stucker, B. (2009). Additive manufacturing technologies: rapid prototyping to direct digital manufacturing: Springer Verlag.

Huang, K., & Goodenough, J. B. (2009). Solid oxide fuel cell technology: principles, performance and operations: Woodhead Publishing.

Larminie, J., Dicks, A., & Knovel. (2003). Fuel cell systems explained.

Lejeune, M., Chartier, T., Dossou-Yovo, C., & Noguera, R. (2009). Ink-jet printing of ceramic micro-pillar arrays. Journal of the European Ceramic Society, 29(5), 905-911.

Li, C. J., Ning, X. J., & Li, C. X. (2005). Effect of densification processes on the properties of plasma-sprayed YSZ electrolyte coatings for solid oxide fuel cells. Surface and Coatings Technology, 190(1), 60-64.

Liao, Y. S., Chen, S. T., Lin, C. S., & Chuang, T. J. (2005). Fabrication of high aspect ratio microstructure arrays by micro reverse wire-EDM. Journal of Micromechanics and Microengineering, 15, 1547.

Menzler, N. H., Tietz, F., Uhlenbruck, S., Buchkremer, H. P., & Stöver, D. (2010). Materials and manufacturing technologies for solid oxide fuel cells. Journal of materials science, 45(12), 3109-3135.

Minh, N., & Montgomery, K. (2004). Tape Calendering Manufacturing Process for Multilayer Thin-Film Solid Oxide Fuel Cells: Hybrid Power Generation Systems (US).

Mistler, R. E., & Twiname, E. R. (2000). Tape Casting: theory and practice: The American Ceramic Society.

Ormerod, R. M. (2002). Solid oxide fuel cells. Chem. Soc. Rev., 32(1), 17-28.

Parody,R (2011) "Design of experiments for scientists and engineers", Rochester Institute of technology.

Piao, J., Sun, K., Zhang, N., & Xu, S. (2008). A study of process parameters of LSM and LSM-YSZ composite cathode films prepared by screen-printing. Journal of Power Sources, 175(1), 288-295.

Rotureau, D., Viricelle, J. P., Pijolat, C., Caillol, N., & Pijolat, M. (2005). Development of a planar SOFC device using screen-printing technology. Journal of the European Ceramic Society, 25(12), 2633-2636.

*S*criven, L. (1988). Physics and applications of dip coating and spin coating. MRS Spring Meeting, 121, 717.

Shao, Z., & Haile, S. M. (1985). A high-performance cathode for the next generation of solid-oxide fuel cells. semiconductors, 124, 161-253.

Simner, S. P., Bonnett, J. F., Canfield, N. L., Meinhardt, K. D., Shelton, J. P., Sprenkle, V. L., et al. (2003). Development of lanthanum ferrite SOFC cathodes. Journal of power sources, 113(1), 1-10.

Simwonis, D., Thulen, H., Dias, F. J., Naoumidis, A., & Stover, D. (1999). Properties of Ni/YSZ porous cermets for SOFC anode substrates prepared by tape casting and coat-mix® process. Journal of Materials Processing Technology, 92, 107-111.

Singhal, S. C. (2000). Advances in solid oxide fuel cell technology. Solid State Ionics, 135(1-4), 305-313.

Singhal, S. C., & Kendall, K. (2003). High temperature solid oxide fuel cells: fundamentals, design, and applications: Elsevier Science.

Sofie, S. W. (2007). Fabrication of Functionally Graded and Aligned Porosity in Thin Ceramic Substrates With the Novel Freeze–Tape-Casting Process. Journal of the American Ceramic Society, 90(7), 2024-2031.

Sukeshini, A. M., Gardner, P., Meisenkothen, F., Jenkins, T., Miller, R., Rottmayer, M., et al. (2011). Aerosol Jet Printing and Microstructure of SOFC Electrolyte and Cathode Layers.

Sukeshini, A. M., Jenkins, T., Gardner, P., Miller, R. M., & Reitz, T. L. (2010). Investigation of Aerosol Jet Deposition Parameters for Printing SOFC Layers. ASME Conference Proceedings, 2010(44045), 325-332.

Van Herle, J., Ihringer, R., Vasquez Cavieres, R., Constantin, L., & Bucheli, O. (2001). Anode supported solid oxide fuel cells with screen-printed cathodes. Journal of the European Ceramic Society, 21(10-11), 1855-1859.

Wang, W. (2005). Fabrication and Performance of GDC-Impregnated (La, Sr) MnO Cathodes for Intermediate Temperature Solid Oxide Fuel Cells. Journal of the Electrochemical Society, 152, A1398.

Weber, A., & Ivers-Tiffée, E. (2004). Materials and concepts for solid oxide fuel cells (SOFCs) in stationary and mobile applications. Journal of Power Sources, 127(1-2), 273-283.

Xia, C., Zha, S., Yang, W., Peng, R., Peng, D., & Meng, G. (2000). Preparation of yttria stabilized zirconia membranes on porous substrates by a dip-coating process. Solid state ionics, 133(3), 287-294.

Xu, X., Xia, C., Huang, S., & Peng, D. (2005). YSZ thin films deposited by spin-coating for IT-SOFCs. Ceramics international, 31(8), 1061-1064.

Appendix A

A1: Preliminary experiment data

Table 17: Initial experiment data table

No.	Feed rate (mm/sec)	Atomizer flow (ccm)	Width (microns)			
			1 pass	3 passes	6 passes	9 passes
1	15	1000	52	68.39	70.9	75.31
2	5	1150	119.3	127	133.52	130.06
3	5	1000	100	100.48	104.13	98.17
4	15	1150	73.77	89.7	96.4	98.5

A2: Screening experiment data

Table 18: Screening experiment data table for width

A	B	C	D	E	F	G	Width	Std. dev.
-1	-1	-1	-1	-1	-1	-1	76.9	0.58
1	-1	-1	-1	1	-1	1	62	1.24
-1	1	-1	-1	1	1	-1	84	0.24
1	1	-1	-1	-1	1	1	118.7	2.41
-1	-1	1	-1	1	1	1	63.9	2.61
1	-1	1	-1	-1	1	-1	116.8	0.95
-1	1	1	-1	-1	-1	1	110.8	0.78
1	1	1	-1	1	-1	-1	112.3	1.81
-1	-1	-1	1	-1	1	1	92	0.34
1	-1	-1	1	1	1	-1	102	0.57
-1	1	-1	1	1	-1	1	93.1	2.75
1	1	-1	1	-1	-1	-1	146	1.50
-1	-1	1	1	1	-1	-1	90	0.82
1	-1	1	1	-1	-1	1	98.6	1.64
-1	1	1	1	-1	1	-1	138.9	2.14
1	1	1	1	1	1	1	88.3	2.30

Table 19: Screening experiment data table for height

A	B	C	D	E	F	G	Height	Std. dev.
-1	-1	-1	-1	-1	-1	-1	3.11	0.50
1	-1	-1	-1	1	-1	1	9.29	2.40
-1	1	-1	-1	1	1	-1	13.13	0.21
1	1	-1	-1	-1	1	1	38.1	2.22
-1	-1	1	-1	1	1	1	8.66	0.43
1	-1	1	-1	-1	1	-1	26.15	3.02
-1	1	1	-1	-1	-1	1	5.31	0.16
1	1	1	-1	1	-1	-1	8.9	1.18
-1	-1	-1	1	-1	1	1	11.66	0.22
1	-1	-1	1	1	1	-1	8.72	0.24
-1	1	-1	1	1	-1	1	3.01	0.82
1	1	-1	1	-1	-1	-1	10.7	1.28
-1	-1	1	1	1	-1	-1	3.11	0.11
1	-1	1	1	-1	-1	1	18.99	1.72
-1	1	1	1	-1	1	-1	11.92	0.18
1	1	1	1	1	1	1	9.27	0.21

Appendix B

B1: Factorial Fit: SQRT Height versus Atomizer flow ra, Delta(ccm), ...

Estimated Effects and Coefficients for SQRT Height (coded units)

Term	Effect	Coef	SE Coef	T	P
Constant		3.2462	0.04872	66.63	0.010
Atomizer flow rate (ccm)	1.2431	0.6216	0.04872	12.76	0.050
Delta(ccm)	0.1534	0.0767	0.04872	1.57	0.360
Cup temp(C)	-0.0024	-0.0012	0.04872	-0.02	0.985
Platen temp(C)	-0.4949	-0.2475	0.04872	-5.08	0.124
Feed rate(mm/sec)	-0.9698	-0.4849	0.04872	-9.95	0.064
Tube temp(C)	1.1864	0.5932	0.04872	12.17	0.052
Sheath flow rate(ccm)	0.2620	0.1310	0.04872	2.69	0.227
Atomizer flow rate (ccm)*Delta(ccm)	-0.1536	-0.0768	0.04872	-1.58	0.360
Atomizer flow rate (ccm)*Cup temp(C)	0.0164	0.0082	0.04872	0.17	0.894
Atomizer flow rate (ccm)* Platen temp(C)	-0.4275	-0.2137	0.04872	-4.39	0.143
Atomizer flow rate (ccm)* Feed rate(mm/sec)	-0.7520	-0.3760	0.04872	-7.72	0.082
Atomizer flow rate (ccm)* Tube temp(C)	-0.2802	-0.1401	0.04872	-2.88	0.213
Atomizer flow rate (ccm)* Sheath flow rate(ccm)	0.3141	0.1570	0.04872	3.22	0.192
Delta(ccm)*Platen temp(C)	-0.4000	-0.2000	0.04872	-4.11	0.152

S = 0.194893 PRESS = 9.72370
R-Sq = 99.82% R-Sq(pred) = 54.56% R-Sq(adj) = 97.34%

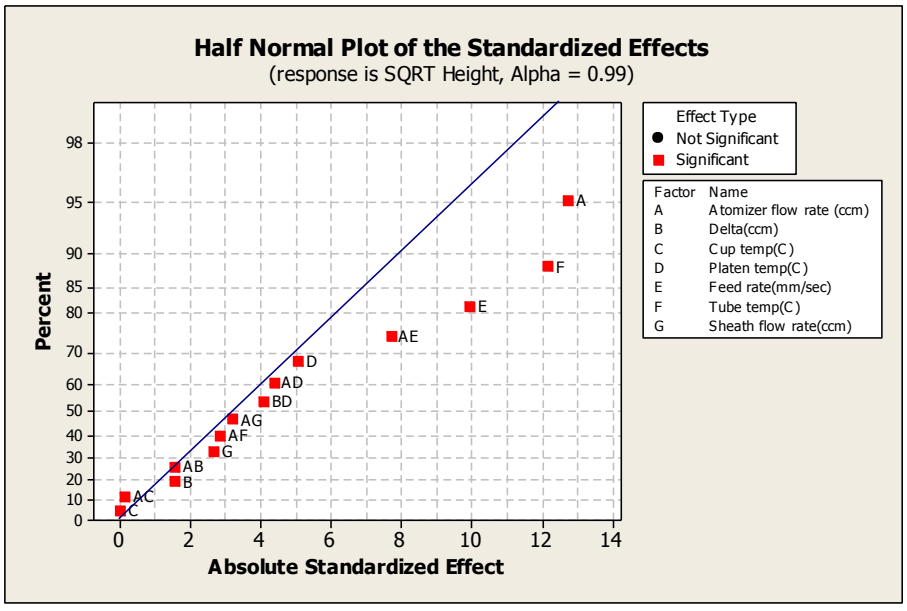

B2: Analysis of Variance for Height (coded units)

Source	DF	Seq SS	Adj SS	Adj MS	F	P
Main Effects	7	16.9217	16.9217	2.41738	63.64	0.096
Atomizer flow rate (ccm)	1	6.1815	6.1815	6.18147	162.74	0.050
Delta(ccm)	1	0.0941	0.0941	0.09411	2.48	0.360
Cup temp(C)	1	0.0000	0.0000	0.00002	0.00	0.985
Platen Temp(C)	1	0.9798	0.9798	0.97977	25.79	0.124
Feed Rate(mm/sec)	1	3.7617	3.7617	3.76173	99.04	0.064
Tube temp(C)	1	5.6300	5.6300	5.62998	148.22	0.052
Sheath flow rate(ccm)	1	0.2746	0.2746	0.27458	7.23	0.227
2-Way Interactions	7	4.4372	4.4372	0.63388	16.69	0.186
Atomizer flow rate (ccm)*Delta(ccm)	1	0.0944	0.0944	0.09436	2.48	0.360
Atomizer flow rate (ccm)*Cup temp(C)	1	0.0011	0.0011	0.00108	0.03	0.894
Atomizer flow rate (ccm)*Platen Temp(C)	1	0.7309	0.7309	0.73087	19.24	0.143
Atomizer flow rate (ccm)*Feed Rate(mm/sec)	1	2.2622	2.2622	2.26224	59.56	0.082
Atomizer flow rate (ccm)*Tube temp(C)	1	0.3140	0.3140	0.31396	8.27	0.213
Atomizer flow rate (ccm)*Sheath flow rate(ccm)	1	0.3945	0.3945	0.39455	10.39	0.192
Delta(ccm)*Platen Temp(C)	1	0.6401	0.6401	0.64011	16.85	0.152
Residual Error	1	0.0380	0.0380	0.03798		
Total	15	21.3968				

B3: Factorial Fit: Width versus Atomizer flow rate (ccm), Delta(ccm), ...

Estimated Effects and Coefficients for Width (coded units)

Term	Effect	Coef	SE Coef	T	P
Constant		99.64	0.9063	109.95	0.006
Atomizer flow rate (ccm)	11.89	5.94	0.9063	6.56	0.096
Delta(ccm)	23.74	11.87	0.9063	13.10	0.049
Cup temp(C)	5.61	2.81	0.9063	3.10	0.199
Platen temp(C)	12.94	6.47	0.9063	7.14	0.089
Feed rate(mm/sec)	-25.39	-12.69	0.9063	-14.01	0.045
Tube temp(C)	1.86	0.93	0.9063	1.03	0.491
Sheath flow rate(ccm)	-17.44	-8.72	0.9063	-9.62	0.066
Atomizer flow rate (ccm)*Delta(ccm)	-2.26	-1.13	0.9063	-1.25	0.430
Atomizer flow rate (ccm)*Cup temp(C)	-8.79	-4.39	0.9063	-4.85	0.129
Atomizer flow rate (ccm)* Platen temp(C)	-6.66	-3.33	0.9063	-3.68	0.169
Atomizer flow rate (ccm)* Feed rate(mm/sec)	-3.49	-1.74	0.9063	-1.92	0.305
Atomizer flow rate (ccm)* Tube temp(C)	-0.14	-0.07	0.9063	-0.08	0.952
Atomizer flow rate (ccm)* Sheath flow rate(ccm)	-9.94	-4.97	0.9063	-5.48	0.115
Delta(ccm)*Platen temp(C)	-2.81	-1.41	0.9063	-1.55	0.364

S = 3.625 PRESS = 3364
R-Sq = 99.84% R-Sq(pred) = 60.04% R-Sq(adj) = 97.66%

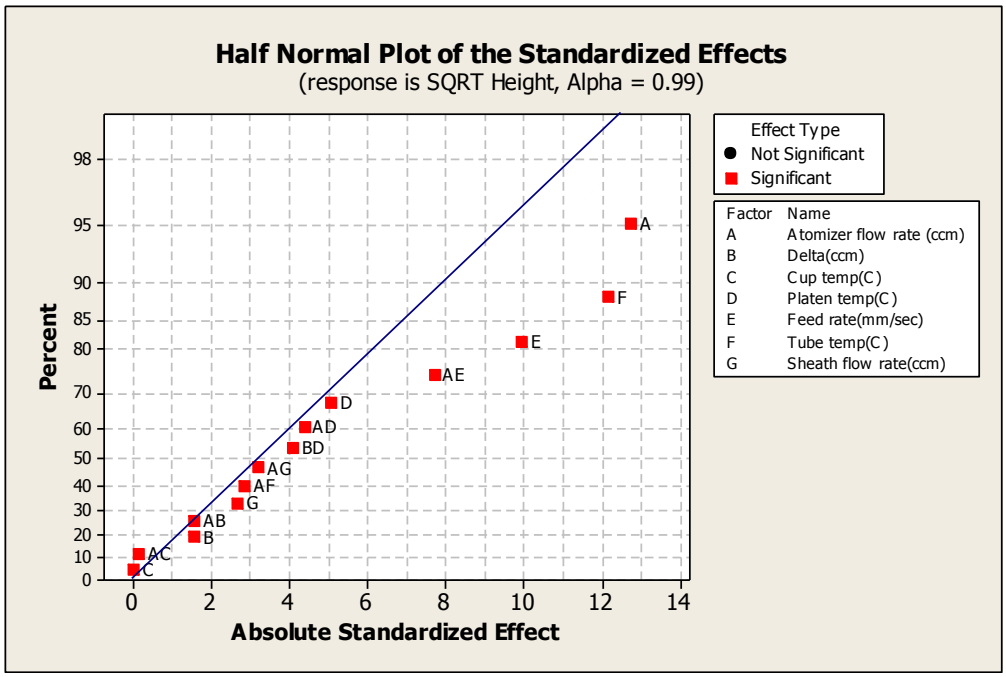

B4: Analysis of Variance for Width (coded units)

Source	DF	Seq SS	Adj SS	Adj MS
Main Effects	7	7422.88	7422.88	1060.41
Atomizer flow rate (ccm)	1	565.25	565.25	565.25
Delta(ccm)	1	2253.88	2253.88	2253.88
Cup temp(C)	1	126.00	126.00	126.00
Platen Temp(C)	1	669.52	669.52	669.52
Feed Rate(mm/sec)	1	2578.10	2578.10	2578.10
Tube temp(C)	1	13.88	13.88	13.88
Sheath flow rate(ccm)	1	1216.27	1216.27	1216.27
2-Way Interactions	7	982.29	982.29	140.33
Atomizer flow rate (ccm)*Delta(ccm)	1	20.48	20.48	20.48
Atomizer flow rate (ccm)*Cup temp(C)	1	308.88	308.88	308.88
Atomizer flow rate (ccm)*Platen Temp(C)	1	177.56	177.56	177.56
Atomizer flow rate (ccm)*Feed Rate(mm/sec)	1	48.65	48.65	48.65
Atomizer flow rate (ccm)*Tube temp(C)	1	0.08	0.08	0.08
Atomizer flow rate (ccm)*Sheath flow rate(ccm)	1	395.02	395.02	395.02
Delta(ccm)*Platen Temp(C)	1	31.64	31.64	31.64
Residual Error	1	13.14	13.14	13.14
Total	15	8418.32		

Source	F	P
Main Effects	80.70	0.086
Atomizer flow rate (ccm)	43.02	0.096
Delta(ccm)	171.52	0.049
Cup temp(C)	9.59	0.199
Platen Temp(C)	50.95	0.089
Feed Rate(mm/sec)	196.19	0.045
Tube temp(C)	1.06	0.491
Sheath flow rate(ccm)	92.56	0.066
2-Way Interactions	10.68	0.232
Atomizer flow rate (ccm)*Delta(ccm)	1.56	0.430
Atomizer flow rate (ccm)*Cup temp(C)	23.51	0.129
Atomizer flow rate (ccm)*Platen Temp(C)	13.51	0.169
Atomizer flow rate (ccm)*Feed Rate(mm/sec)	3.70	0.305
Atomizer flow rate (ccm)*Tube temp(C)	0.01	0.952
Atomizer flow rate (ccm)*Sheath flow rate(ccm)	30.06	0.115
Delta(ccm)*Platen Temp(C)	2.41	0.364
Residual Error		
Total		

Appendix C

C1: General Regression Analysis for SQRT height

Regression Equation

Sqrt. height = 3.24622 + 0.621564 Atomizer flow rate (ccm) + 0.593189 Tube temp(C) - 0.48488 Feed Rate(mm/sec) - 0.376019 Atomizer flow rate (ccm)*Feed Rate(mm/sec)

Coefficients

Term	Coef	SE Coef	T	P
Constant	3.24622	0.0769487	42.1868	0.000
Atomizer flow rate (ccm)	0.62156	0.0769487	8.0776	0.000
Tube temp(C)	0.59319	0.0769487	7.7089	0.000
Feed Rate(mm/sec)	-0.48488	0.0769487	-6.3013	0.000
Atomizer flow rate (ccm)*Feed Rate(mm/sec)	-0.37602	0.0769487	-4.8866	0.000

Summary of Model

S = 0.533117 R-Sq = 81.41% R-Sq(adj) = 79.68%
PRESS = 15.2285 R-Sq(pred) = 76.83%

Analysis of Variance

Source	DF	Seq SS	Adj SS	Adj MS	F	P
Regression	4	17.8354	17.8354	4.45886	13.7720	0.0002911
Atomizer flow rate (ccm)	1	6.1815	6.1815	6.18147	19.0926	0.0011185
Feed Rate(mm/sec)	1	3.7617	3.7617	3.76173	11.6188	0.0058393
Tube temp(C)	1	5.6300	5.6300	5.62998	17.3892	0.0015626
Atomizer flow rate (ccm)*Feed Rate(mm/sec)	1	2.2622	2.2622	2.26224	6.9874	0.0228557
Error	11	3.5614	3.5614	0.32376		
Lack-of-Fit	3	2.0246	2.0246	0.67486	3.5131	0.0689508
Pure Error	8	1.5368	1.5368	0.19210		
Total	15	21.3968				

Residual Plots for SQRT HEIGHT

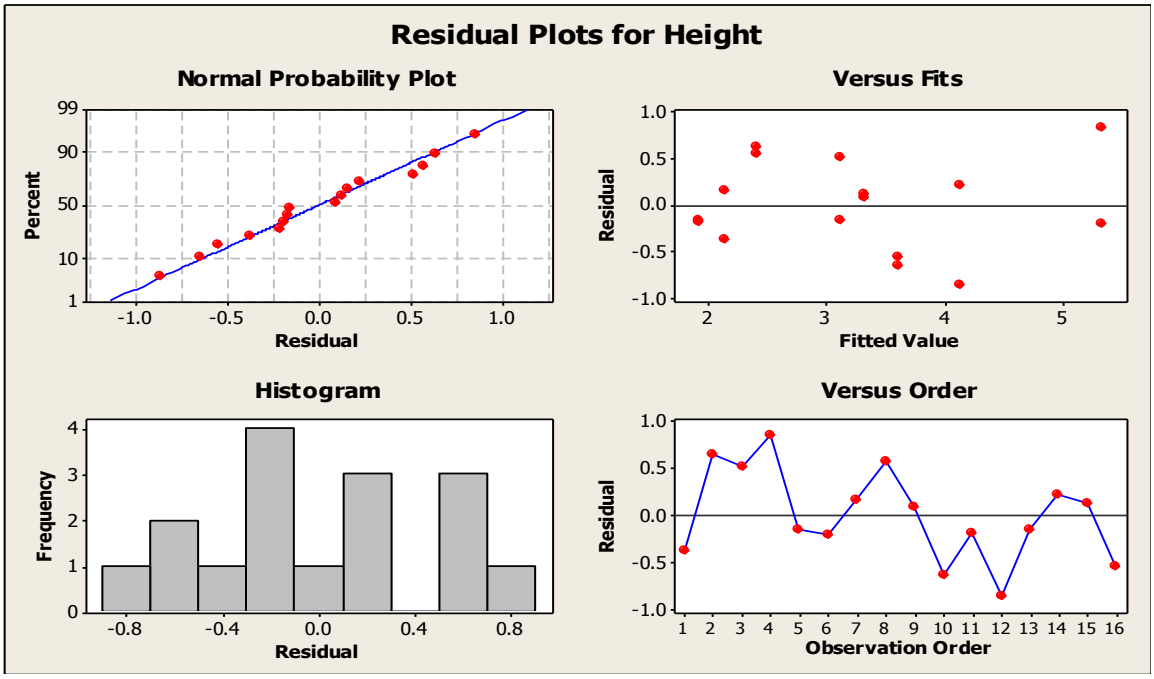

Probability Plot of Residuals for SQRT Height

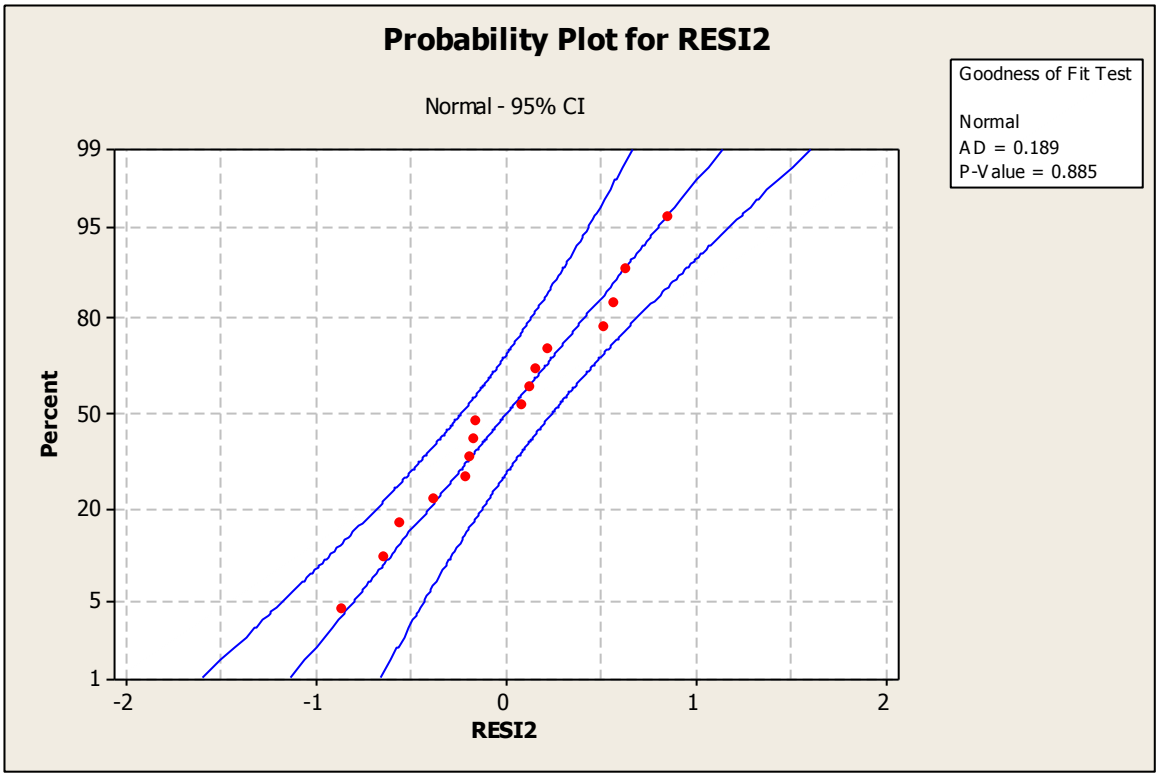

Main Effects Plot for SQRT HEIGHT

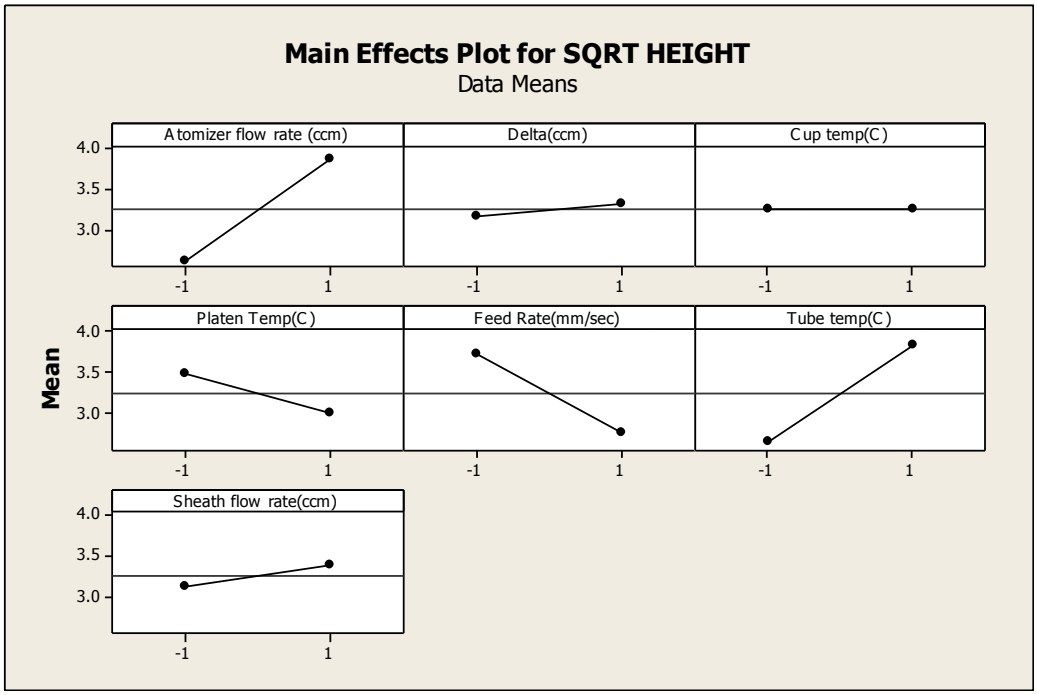

Interaction Plot for SQRT HEIGHT

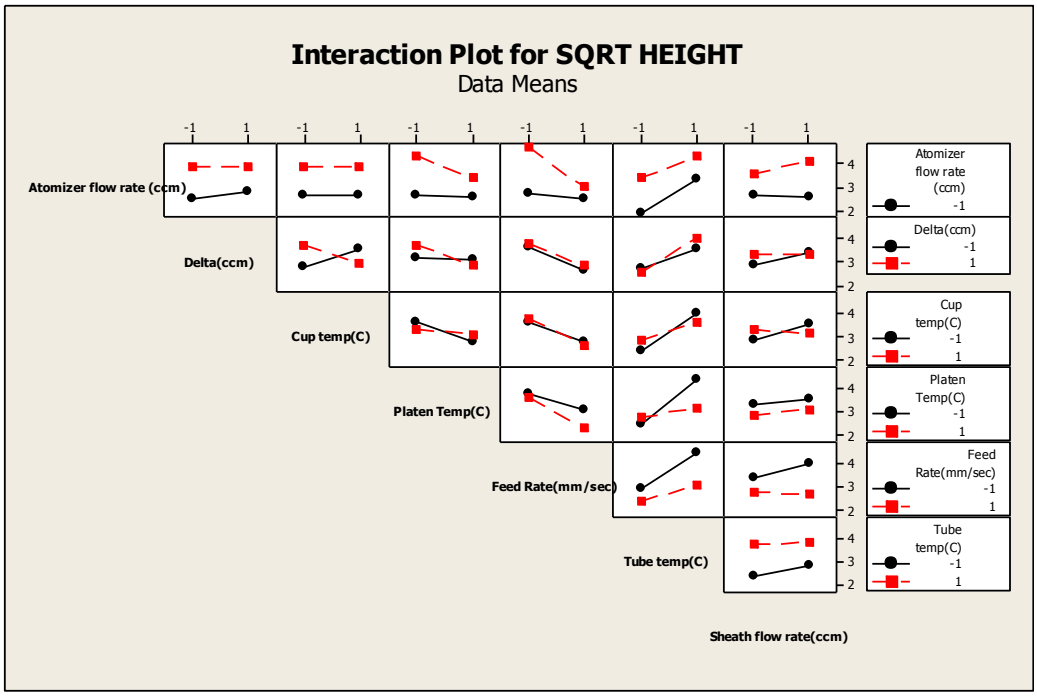

C2: General Regression Analysis for Width

Regression Equation

Width = 99.6437 + 11.8688 Delta(ccm) - 12.6937 Feed Rate(mm/sec) - 8.71875 Sheath flow rate(ccm)

Coefficients

Term	Coef	SE Coef	T	P
Constant	99.6437	3.51342	28.3609	0.000
Delta(ccm)	11.8688	3.51342	3.3781	0.005
Feed Rate(mm/sec)	-12.6937	3.51342	-3.6129	0.004
Sheath flow rate(ccm)	-8.7188	3.51342	-2.4816	0.029

Summary of Model

S = 14.0537 R-Sq = 71.85% R-Sq(adj) = 64.81%
PRESS = 4213.47 R-Sq(pred) = 49.95%

Analysis of Variance

Source	DF	Seq SS	Adj SS	Adj MS	F	P
Regression	3	6048.24	6048.24	2016.08	10.2077	0.001272
Delta(ccm)	1	2253.88	2253.88	2253.88	11.4117	0.005487
Feed Rate(mm/sec)	1	2578.10	2578.10	2578.10	13.0532	0.003560
Sheath flow rate(ccm)	1	1216.27	1216.27	1216.27	6.1581	0.028876
Error	12	2370.08	2370.08	197.51		
Lack-of-Fit	4	1010.11	1010.11	252.53	1.4855	0.293219
Pure Error	8	1359.96	1359.96	170.00		
Total	15	8418.32				

Fits and Diagnostics for Unusual Observations

Obs	Width	Fit	SE Fit	Residual	St Resid	
1	76.9	109.187	7.02685	-32.2875	-2.65285	R

Residual Plots for SQRT Width

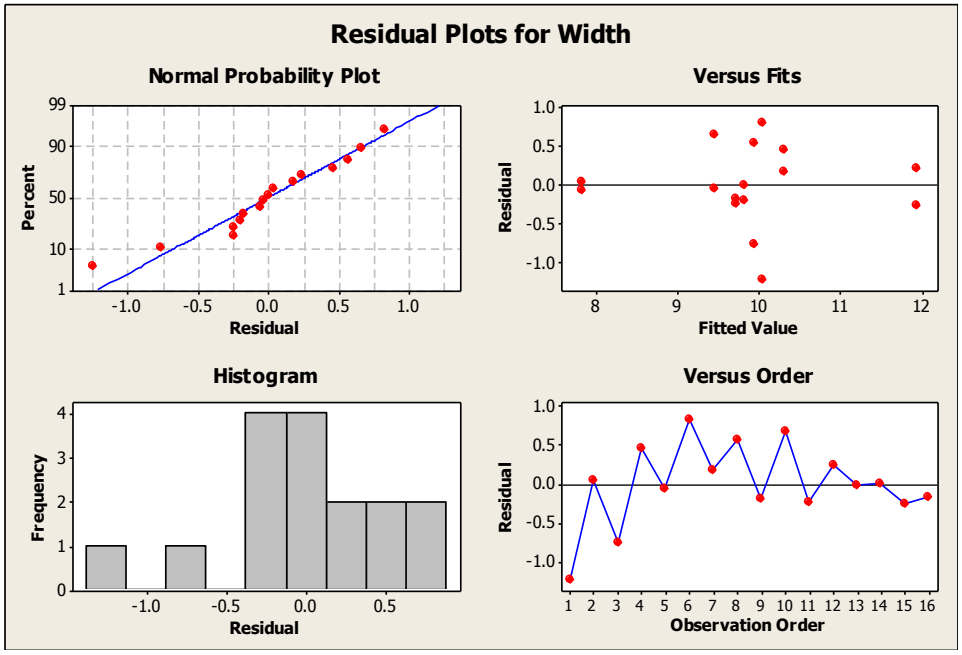

Main Effects Plot for SQRT WIDTH

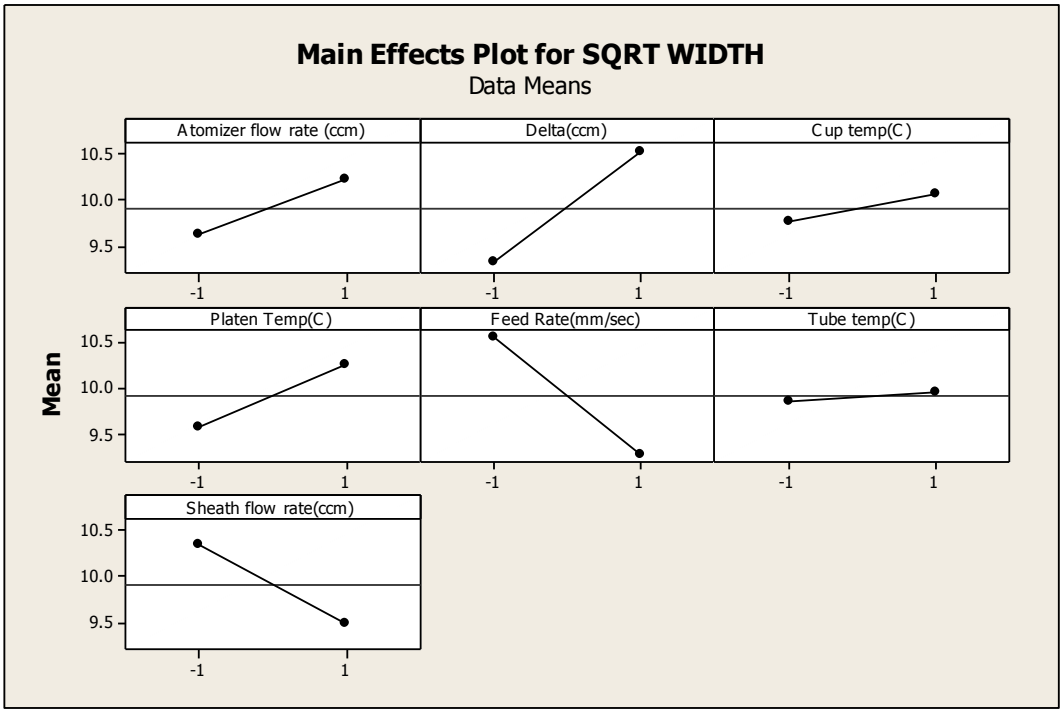

Interaction Plot for SQRT WIDTH

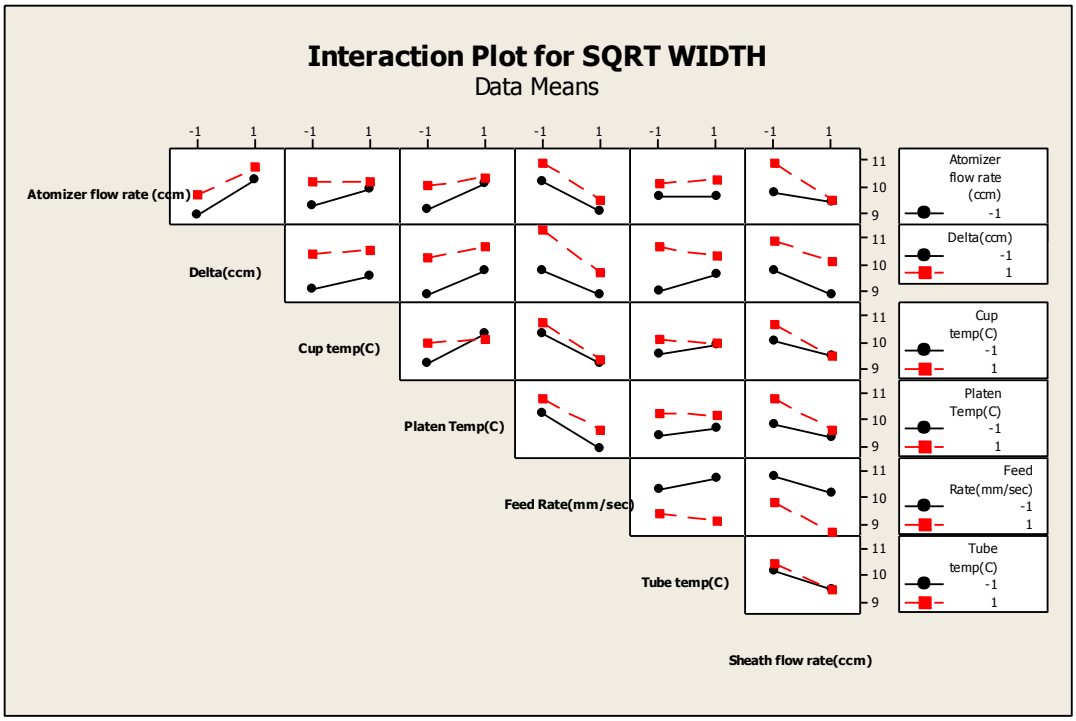

C3: ANOVA for Width Higher Order Model

Coefficients

Term	Coef	SE Coef	T	P
Constant	94.6630	2.69362	35.1434	0.000
feed rate	-9.2722	1.24690	-7.4362	0.000
sheath	-8.9722	1.24690	-7.1956	0.000
delta	10.7444	1.24690	8.6169	0.000
feed rate*sheath	-1.8750	1.52714	-1.2278	0.236
feed rate*delta	-1.4167	1.52714	-0.9277	0.367
sheath*delta	4.1917	1.52714	2.7448	0.014
feed rate*feed rate	4.2278	2.15970	1.9576	0.067
sheath*sheath	0.7278	2.15970	0.3370	0.740
delta*delta	-0.2556	2.15970	-0.1183	0.907

Summary of Model

S = 5.29017 R-Sq = 91.99% R-Sq(adj) = 87.75%
PRESS = 1227.02 R-Sq(pred) = 79.34%

Analysis of Variance

Source	DF	Seq SS	Adj SS	Adj MS	F	P
Regression	9	5462.45	5462.45	606.94	21.6873	0.000000
feed rate	1	1547.53	1547.53	1547.53	55.2969	0.000001
sheath	1	1449.01	1449.01	1449.01	51.7766	0.000001
delta	1	2077.98	2077.98	2077.98	74.2508	0.000000
feed rate*sheath	1	42.19	42.19	42.19	1.5075	0.236257
feed rate*delta	1	24.08	24.08	24.08	0.8606	0.366568
sheath*delta	1	210.84	210.84	210.84	7.5338	0.013818
feed rate*feed rate	1	107.24	107.24	107.24	3.8321	0.066904
sheath*sheath	1	3.18	3.18	3.18	0.1136	0.740256
delta*delta	1	0.39	0.39	0.39	0.0140	0.907194
Error	17	475.76	475.76	27.99		
Total	26	5938.21				

Fits and Diagnostics for Unusual Observations

No unusual observations

C4: General Regression Analysis for width

Regression Equation

width = 94.9778 - 9.27222 feed rate - 8.97222 sheath + 10.7444 delta + 4.19167 Sheath*Delta + 4.22778 Feed^2

Coefficients

Term	Coef	SE Coef	T	P
Constant	94.9778	1.69905	55.9005	0.000
feed rate	-9.2722	1.20141	-7.7178	0.000
sheath	-8.9722	1.20141	-7.4681	0.000
delta	10.7444	1.20141	8.9432	0.000
Sheath*Delta	4.1917	1.47142	2.8487	0.010
Feed^2	4.2278	2.08090	2.0317	0.055

Summary of Model

S = 5.09716 R-Sq = 90.81% R-Sq(adj) = 88.62%
PRESS = 913.982 R-Sq(pred) = 84.61%

Analysis of Variance

Source	DF	Seq SS	Adj SS	Adj MS	F	P
Regression	5	5392.61	5392.61	1078.52	41.5120	0.0000000
feed rate	1	1547.53	1547.53	1547.53	59.5641	0.0000001
sheath	1	1449.01	1449.01	1449.01	55.7721	0.0000002
delta	1	2077.98	2077.98	2077.98	79.9806	0.0000000
Sheath*Delta	1	210.84	210.84	210.84	8.1152	0.0096167
Feed^2	1	107.24	107.24	107.24	4.1278	0.0550287
Error	21	545.60	545.60	25.98		
Total	26	5938.21				

Fits and Diagnostics for Unusual Observations

No unusual observations

Residual Plots for width

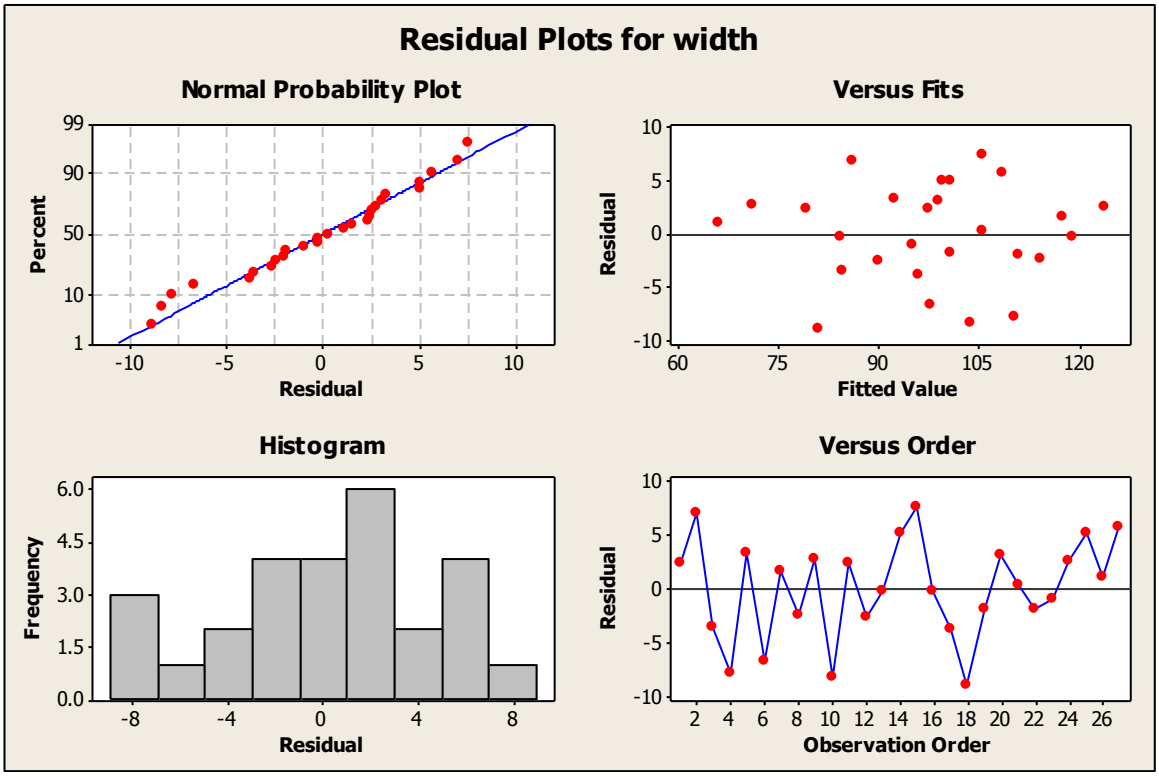

Appendix D

D1: Sample Optomec code for generating a single column of eight adjacent pillars.

```
! *********************************
! FID1 0,0
! FID  END
! Generated by: Virtual Masking ® Tools v1.84
! Axes: XYZTR=XY---
! Resolution: 4000,4000,-,-,-
! C:\Documents and Settings\OPTOMEC INC\Desktop\Toolpaths\niranjan\col1.dxf
! *********************************

ptp/e XY,0,0
OUT0.0=1
wait 3
ptp/e XY,0,4
wait 4000
till (^X_AST.#MOVE) & (^Y_AST.#MOVE)
OUT0.0=0

ptp/e XY,0,480
OUT0.0=1
wait 3
ptp/e XY,0,484
wait 4000
till (^X_AST.#MOVE) & (^Y_AST.#MOVE)
OUT0.0=0
```

```
ptp/e XY,0,960
OUT0.0=1
wait 3
ptp/e XY,0,964
wait 4000
till (^X_AST.#MOVE) & (^Y_AST.#MOVE)
OUT0.0=0

ptp/e XY,0,1440
OUT0.0=1
wait 3
ptp/e XY,0,1444
wait 4000
till (^X_AST.#MOVE) & (^Y_AST.#MOVE)
OUT0.0=0

ptp/e XY,0,1920
OUT0.0=1
wait 3
ptp/e XY,0,1924
wait 4000
till (^X_AST.#MOVE) & (^Y_AST.#MOVE)
OUT0.0=0
```

```
ptp/e XY,0,2400
OUT0.0=1
wait 3
ptp/e XY,0,2404
wait 4000
till (^X_AST.#MOVE) & (^Y_AST.#MOVE)
OUT0.0=0

ptp/e XY,0,2880
OUT0.0=1
wait 3
ptp/e XY,0,2884
wait 4000
till (^X_AST.#MOVE) & (^Y_AST.#MOVE)
OUT0.0=0

ptp/e XY,0,3360
OUT0.0=1
wait 3
ptp/e XY,0,3364
wait 4000
till (^X_AST.#MOVE) & (^Y_AST.#MOVE)
OUT0.0=0
```